The Astrophysical Journal, 897:165 (24pp), 2020 July 10 https://doi.org/10.3847/1538-4357/ab99c1

Bayesian Inference of Dense Matter Equation of State within Relativistic Mean Field Models Using Astrophysical Measurements

Silvia Traversi[1,2], Prasanta Char[2], and Giuseppe Pagliara[1,2]
[1] Dipartimento di Fisica e Scienze della Terra, Università di Ferrara, Via Saragat 1, I-44122 Ferrara, Italy
[2] INFN Sezione di Ferrara, Via Saragat 1, I-44122 Ferrara, Italy; char@fe.infn.it
Received 2020 February 24; revised 2020 May 15; accepted 2020 June 1; published 2020 July 15

Abstract

We present a Bayesian analysis to constrain the equation of state of dense nucleonic matter by exploiting the available data from symmetric nuclear matter at saturation, observations of compact X-ray sources, and the gravitational wave event GW170817. For the first time, such an analysis is performed by using a class of models, the relativistic mean field models, that allow one to consistently construct an equation of state in a wide range of densities, isospin asymmetries, and temperatures. The selected class of models contains five nuclear physics empirical parameters at saturation for which we construct the joint posterior distributions. By exploring different types of priors, we find that the equations of state with the largest evidence are the ones featuring a strong reduction of the effective mass of the nucleons in dense matter, which can be interpreted as an indication of a phase transition to a chiral symmetry restored phase. Those equations of state, in turn, predict $R_{1.4} \sim 12$ km. Finally, we present a preliminary investigation of the effect of including Λ hyperons, showing that they appear in stars more massive than about 1.6 $M_{\odot}$ and lead to radii larger than about $R_{1.4} \sim 14$ km. Within the model explored here, the formation of such particles provides poor agreement with the constraints from GW170817.

Unified Astronomy Thesaurus concepts: Bayesian statistics (1900); Neutron stars (1108); Nuclear astrophysics (1129); Neutron star cores (1107)

Supporting material: figure set

1. Introduction

A neutron star (NS), born in the aftermath of a core-collapse supernova explosion, can sustain densities above a few times the nuclear saturation density in its interior (Glendenning 1997). The composition and properties of matter are largely unknown at such densities. The data available from laboratory experiments and ab initio calculations provide the descriptions of the equation of state (EOS) of symmetric nuclear matter at the nuclear saturation density. Then, the EOS is extrapolated using available theoretical models to describe the properties of matter at supranuclear densities and high-isospin asymmetries but remains largely model-dependent. Fortunately, we have a plethora of astronomical observations that can help to constrain the EOS for NS matter (see Lattimer & Prakash 2007; Oertel et al. 2017, for a review). Since one can have a unique map from the pressure–energy density relation to the mass–radius diagram by solving the Tolman–Oppenheimer–Volkoff (TOV) equations, the measurements of masses and radii can provide valuable insights on the EOS at that density regime. Presently, we have precise observations of masses for several massive NSs (Demorest et al. 2010; Antoniadis et al. 2013; Fonseca et al. 2016; Arzoumanian et al. 2018; Cromartie et al. 2019). The observations of pulsars heavier than 2 $M_{\odot}$ have put a very strong lower limit on the maximum mass and already ruled out many soft EOSs. There exist a few independent observations for NS radii as well, from the thermonuclear bursts emitted by accreting NSs and the thermal emission of low-mass X-ray binaries in quiescence (qLMXBs; Guillot et al. 2013; Özel et al. 2016; Özel & Freire 2016; Nättilä et al. 2017). Most recently, the NICER collaboration has also reported a very accurate joint measurement of the mass and radius of the millisecond pulsar PSR J0030+0451 (Miller et al. 2019; Riley et al. 2019a). In 2017, the LIGO-VIRGO collaboration (LVC) reported the first ever detection of gravitational waves (GWs) from a binary NS (BNS) merger event, GW170817, which provided an estimate of the combined tidal deformability for the components of the binary (Abbott et al. 2017, 2018). The tidal deformability and radii measurements tend to prefer more compact stars; therefore, several stiff EOSs have been ruled out. In this regard, future observations from NICER and other X-ray missions, such as eXTP (Watts et al. 2019), will be able to provide simultaneous measurements of mass and radius with better accuracy, thus allowing one to obtain even stronger constraints on the EOS.

In recent years, since the seminal work of Steiner et al. (2010), substantial progress has been made to provide a statistical inference on the EOS models in light of the available astrophysical data and experimental laboratory data. The Bayesian method is appropriate in this context because it allows one to naturally include the a priori knowledge on the low-density and symmetric EOS and to explore, in a controlled way, the wide space of parameters that determine the NS EOS. The new paradigm, proposed in Steiner et al. (2010), is to match the low-density EOS (which is constrained by theoretical and experimental nuclear physics) with parameterized high-density EOSs. A very simple choice is to use piecewise polytropic EOSs, since, with a few parameters (for instance, the adiabatic indices and the densities of matching), one can reproduce within a small error most of the proposed theoretical calculations of EOSs available in the literature (Read et al. 2009). Interestingly, these parameterizations can also be constrained in the very high-density regime for which perturbative QCD calculations are available (Kurkela et al. 2014). A second possibility is to use the so-called spectral representation of the EOS, which is based on a series expansion of the adiabatic index (Lindblom 2010; Fasano et al. 2019).

Also in this case, few terms in the series are needed in order to capture the high variability of the theoretical EOSs. Recently, a new scheme was adopted in Capano et al. (2020), in which χEFT results are adopted up to twice saturation density and a sampling of the speed of sound values is performed for larger densities. A nonparametric inference approach was followed instead in Essick et al. (2020), the major advantage being the possibility of directly generating the EOS without the need for parameters such as adiabatic indices and/or speed of sound at specific values of the density. Finally, machine-learning techniques were also starting to be used in Fujimoto et al. (2018, 2020) and Ferreira & Providência (2019).

Another powerful method proposed in the literature is the metamodeling of Margueron et al. (2018a, 2018b), where the EOS is built up from a Taylor expansion of the energy per baryon from saturation to high-density and high-isospin asymmetries. Clearly, those methods have advantages and drawbacks: the metamodeling offers the possibility to fully exploit the experimental results on symmetry energy and its density dependence and compute the composition of beta stable matter, in particular the proton fraction, which in turn allows one to constrain the EOS not only via masses, radii, and tidal deformabilities but also with NS cooling data. This aspect is completely neglected within piecewise polytropic and spectral approaches in which only the structure of NSs can be computed. Also, these parameterizations do not contain any aspect of the physics of the symmetry energy. On the other hand, the scheme proposed in Margueron et al. (2018a, 2018b) deals with nonrelativistic nucleons; therefore, it cannot mimic (in the present version) either the appearance of new degrees of freedom (such as hyperons) or a possible phase transition to new phases, such as quark matter (see Alvarez-Castillo et al. 2016, for instance). Phase transitions can, on the other hand, be included, e.g., in piecewise polytropic methods. Indeed, some sources can be better modeled with strong phase transitions, as found in Steiner et al. (2018).

In this paper, we propose an alternative scheme for a statistical inference of the EOS based on a class of relativistic mean field (RMF) models in which the interaction between baryons is mediated by the exchange of scalar and vector mesons. These models, which are extensions of the Walecka model, have been largely adopted for the calculations of finite nuclei and the modeling of the EOS within a wide range of densities, temperatures, and chemical compositions. Many supernova and merger simulations have indeed used those kinds of EOSs, such as the SFHo (Steiner et al. 2013), BHB$\Lambda\phi$ (Banik et al. 2014), and TM1 models (Shen et al. 1998). The advantages of such models are that they can encode the constraints from symmetry energy and finite nuclei, they can easily include hyperons and other possible baryons, and the chemical composition and its impact on the cooling can be studied. In particular, one can include the (little) information we have from the experimental data on hypernuclei. These models have also been confronted recently with the GW data (Malik et al. 2018; Lourenço et al. 2019; Nandi et al. 2019). Another aspect concerns phase transitions; the mean field equation for the σ field is a nonlinear equation that could mimic the occurrence of a phase transition if one uses the nucleon effective mass as an order parameter. As we will discuss later, a rapid drop of the effective mass as a function of the baryon density could be interpreted as suggesting partial restoration of chiral symmetry and thus a likely phase transition to quark matter. Another interesting aspect is that, once the zero-temperature EOS has been constrained by NS observations, one can extend it to finite temperatures and test it for studies of transient phenomena, such as merger and supernova events.

Concerning the astrophysical data, we use a larger data set in our Bayesian analysis with respect to previous works. In particular, we have included the data for the six thermonuclear bursters and five qLMXBs from Özel et al. (2016), one X-ray source of Nättilä et al. (2017), and the two components of GW170817 (Abbott et al. 2018). We also include the recent NICER observations of PSR J0030+0451.

The paper is organized as follows. In Section 2, we introduce the RMF parameterization we adopt for performing the Bayesian analysis. In Section 3, after a brief review of the method, we present the different priors on the EOS and the astrophysical data that will be adopted for constructing the likelihood. In Section 4 we present our results, and in Section 5 we give the discussion and conclusions. In the Appendix, we provide further details of our calculations.

2. Equation of State

The class of RMF models we adopt in this paper is the nonlinear Walecka model proposed in the seminal papers of Boguta & Bodmer (1977) and Glendenning & Moszkowski (1991), which is characterized by the presence of cubic and quartic self-interaction terms for the scalar field σ. Those two terms have been added to the Walecka model in order to keep the values of incompressibility and effective mass at saturation under control (Boguta & Bodmer 1977). The Lagrangian of the model is given by

$$\begin{aligned}\mathcal{L}_B = \sum_B \bar{\Psi}_B (i\gamma_\mu \partial^\mu - m_B + g_{\sigma B}\sigma \\ - g_{\omega B}\gamma_\mu \omega^\mu - g_{\rho B}\gamma_\mu \tau \cdot \rho^\mu)\Psi_B \\ + \frac{1}{2}(\partial_\mu \sigma \partial^\mu \sigma - m_\sigma^2 \sigma^2) \\ - \frac{1}{3} b m_n (g_\sigma \sigma)^3 - \frac{1}{4} c (g_\sigma \sigma)^4 \\ - \frac{1}{4}\omega_{\mu\nu}\omega^{\mu\nu} + \frac{1}{2} m_\omega^2 \omega_\mu \omega^\mu \\ - \frac{1}{4}\rho_{\mu\nu} \cdot \rho^{\mu\nu} - \frac{1}{2} m_\rho^2 \rho_\mu \cdot \rho^\mu, \end{aligned} \quad (1)$$

where σ, ω, and ρ represent the scalar, vector, and vector-isovector mesons, respectively.

The model contains five unknown parameters: g_σ/m_σ, g_ω/m_ω, g_ρ/m_ρ, b, and c. These quantities are related algebraically to five saturation properties of symmetric nuclear matter, i.e., the binding energy per nucleon (E_0), the saturation density (n_0), the symmetry energy (S), the incompressibility (K), and the effective mass of the nucleon (m^*; Glendenning 1997). Hence, we can effectively parameterize our EOS in terms of the aforementioned empirical nuclear physics parameters. We do not report here the expressions for the mean field equations and the thermodynamical quantities that can be found in many references; see, e.g., Glendenning (1997). The model can be easily extended to include hyperons. We consider here only the case of the Λ hyperon, whose experimental value for the potential depth is fixed to -28 MeV, as in Glendenning & Moszkowski (1991). The coupling with the ω meson is set to its SU(3) symmetry value, i.e., $2/3 g_\omega/m_\omega$ (Weissenborn et al. 2012a), whereas the coupling with the σ

meson is directly derived from the potential depth. In this paper, for the Bayesian analysis with the inclusion of hyperons, we do not vary the potential depth or the coupling with the ω meson beyond flavor symmetry, as in Weissenborn et al. (2012a). Thus, we just want to study the effect on the posterior of switching on Λ. In a forthcoming paper, we will also investigate the effects of changing those couplings and including all of the baryons of the octet.

A major drawback of this model is that it cannot include other saturation properties, such as the slope of the symmetry energy L or higher-order derivatives (curvature $K_{\rm sym}$ and skewness $J_{\rm sym}$), which are shown to be relevant in Xie & Li (2019) in the density range up to $2.5n_0$. In particular, in our parameterization, L is a derived quantity and correlated with S. We anticipate that in some of our results, it will come out that L is larger than the typical values proposed in the literature, i.e., $40\,\mathrm{MeV} \lesssim L \lesssim 60\,\mathrm{MeV}$ (see Lattimer & Lim 2013; Xie & Li 2019, for details). The tidal deformability of GW170817 also seems to suggest even smaller values, with the range of L extending down to 9 MeV (Raithel & Özel 2019), thus pointing to significant tension with laboratoty data on neutron skin thickness (see Fattoyev et al. 2018, for a discussion). In principle, to include such quantities, one would need to introduce other interaction terms (including meson mixing terms as in Steiner et al. 2013) or density dependent couplings as in Typel & Wolter (1999) at the cost of losing the direct analytical expressions connecting the parameters of the model and the saturation properties. We postpone such an extension of our work for a future paper. Another drawback is connected with the sign of the quartic coupling c. In several accepted parameterizations, it is negative, thus making the energy unbounded from below for a large value of the σ field. A common viewpoint concerning this issue is to consider the model as an effective model that cannot be extrapolated to arbitrarily high densities and to check for well-behaved EOSs (causality limit and absence of mechanical and chemical instabilities) in the density regime of compact stars. Again, this problem could be addressed in future studies by using hadronic chiral models, such as in Bonanno & Drago (2009).

3. Bayesian Analysis

In Bayesian parameter estimation, the probability distribution of a set of model parameters $\boldsymbol{\theta}$, called the posterior density function (PDF), given data (D) for some model (M) is inferred by the Bayes theorem,

$$P(\boldsymbol{\theta}|D, M) = \frac{P(D|\boldsymbol{\theta}, M)P(\boldsymbol{\theta}|M)}{P(D|M)}, \tag{2}$$

where $P(\boldsymbol{\theta}|M)$ is the prior probability of the parameter set $\boldsymbol{\theta}$. This is updated by the experimental data through the likelihood function, $P(D|\boldsymbol{\theta}, M)$. The denominator, $P(D|M)$, is known as evidence for the model M, which is a constant for the given data D. Since it does not depend on the model parameters, the evidence can be treated as a normalization factor for the posterior. In this work, we mainly follow the Bayesian methodology developed by Steiner et al. (2010), Özel et al. (2016), and Raithel et al. (2017), which is described in the following.

Our parameter set $\boldsymbol{\theta}$ consists of the empirical parameters: $\{m^*, K, n_0, S, E_0\}$. In order to calculate the posterior over $P(\boldsymbol{\theta})$ using the mass–radius distributions ${}_{Pi}(M, R)$ for the $N = 15$ sources we have used in our analysis (see next section), we can write

$$P(m^*, K, n_0, S, E_0|\mathrm{data}) = CP(\mathrm{data}|m^*, K, n_0, S, E_0) \times P(m^*)P(K)P(n_0)P(S)P(E_0), \tag{3}$$

where C is the normalization constant; $P(m^*)$, $P(K)$, $P(n_0)$, $P(S)$, and $P(E_0)$ are the priors over the empirical parameters; and

$$P(\mathrm{data}|m^*, K, n_0, S, E_0) = \prod_{i=1}^{N} P_i(M_i, R_i|m^*, K, n_0, S, E_0) \tag{4}$$

is the likelihood of generating N mass–radius observations given a particular set of empirical parameters. To compute the probability of the realization of (M, R) for a particular source given an EOS, we follow the procedure suggested by Raithel et al. (2017). We take a set of parameters and calculate the couplings using the algebraic relations. Then, we solve the mean field equations to construct the EOS. Using the EOS, we solve the TOV equations and build a mass–radius curve up to the maximum mass that corresponds to the last stable point of the curve. After that, we compute the probability of each configuration of the curve using the M–R distribution of the source. Finally, we assign to the parameter set the maximum probability obtained for the configurations as

$$P_i(M_i, R_i|m^*, K, n_0, S, E_0) = P_{\max}(M_i, R_i|m^*, K, n_0, S, E_0, \rho_c), \tag{5}$$

where the mass–radius curve for a given EOS is parameterized by the central energy density (ρ_c) of the star. We use Markov Chain Monte Carlo (MCMC) simulations to populate the posterior distribution of Equation (3) using the python `emcee` package with a stretch-move algorithm (Foreman-Mackey et al. 2013). Next, we calculate the evidence to compare between different models by performing a Monte Carlo integration over the posterior. We also compute the Bayesian information criterion (BIC) using the standard definition, $\mathrm{BIC} \equiv -2\ln\mathcal{L}_{\max} + k\ln N$, where $\mathcal{L}_{\max}$ is the maximum likelihood, k is the number of parameters, and N is the number of data points.

3.1. Conditions on the Priors

The choice of priors plays an important role in interpreting the data within the domain of a model. Ambiguities in the priors can alter the shape of the posteriors and, consequently, the model predictions (Steiner et al. 2016). Therefore, we need to study the effects of different prior types and ranges. These priors essentially encompass our assumptions for the model. Hence, they can be treated as individual models by themselves, and we compute the Bayes factors (BFs) between every pair of them for a quantitative comparison. We categorize our priors into two different classes: informed and agnostic. For the first class, we choose our priors based on the available constraints from laboratory experiments on the nuclear empirical parameters. For the agnostic priors, we relax those constraints and allow the parameters to be determined mainly from the requirements of the astrophysical data. We implement both Gaussian and uniform priors to investigate their effects on the parameter estimation. In particular, we take five different priors motivated by several different studies in literature (Lattimer &

Table 1
List of the Priors We Employ in This Work

Priors	Range	m^*	K (MeV)	n_0 (fm^{-3})	S (MeV)	B/A (MeV)
Baseline	Min	0.7	200	0.14	28	−16.5
	Max	0.8	300	0.16	35	−16.0
Marg_unif	Min	0.64	219	0.145	31.19	−16.35
	Max	0.71	355	0.153	38.71	−16.12
Marg_Gauss	Mean	0.67	268	0.1494	35.11	−16.24
	σ	0.02	34	0.0025	2.63	0.06
Wide_unif	Min	0.55	172.23	0.145	17.38	−17.03
	Max	0.8	421.02	0.173	50.0	−13.78
Wide_Gauss	Mean	0.708	245.29	0.152	34.11	−16.17
	σ	0.079	39.30	0.004	4.42	0.36

Lim 2013; Dutra et al. 2014; Oertel et al. 2017; Margueron et al. 2018a).

Baseline. The prior ranges are inspired by the results of laboratory experiments. We take the ranges of m^*, K from Glendenning (1997) and S from Lattimer & Lim (2013). Additionally, we choose a sensible range for both n_0 and E_0.

Marg_unif. Following Table 11 of Margueron et al. (2018a) concerning the RMF models, we define a uniform prior with the minimum and maximum value of the parameters of our interest. Those models were chosen among a wider class of RMF models for their ability to provide sensible results for a large number of nuclear properties.

Marg_Gauss. From the aforementioned table of Margueron et al. (2018a), we take the mean and standard deviation of our parameters to define a Gaussian prior.

Wide_unif. We consider the type 2 EOSs of Table 7 of Dutra et al. (2014) and define a uniform prior over the maximum and minimum values of the parameters. We consider only the type 2 EOSs because those correspond to the RMF model with the same scalar self-interactions as in our case. We remark that not all the models of this table are compatible with modern nuclear physics constraints, particularly concerning the symmetry energy.

Wide_Gauss. We consider again the type 2 EOSs of Table 7 of Dutra et al. (2014) and parameterize the uncertainties with Gaussian distributions. In this case, the standard deviations are somewhat larger than the Marg_Gauss.

The corresponding ranges of the empirical parameters for the priors mentioned above are listed in Table 1.

Additionally, we impose the following physical constraints and observational requirements on the EOSs that we construct using the priors.

i. The EOSs should be mechanically stable.
ii. The EOSs must remain causal for the range of densities of our interest.
iii. The maximum stable mass produced by each EOS must be compatible with the observations. In this work, we impose the condition that it must exceed 2 $M_\odot$, as in Güven et al. (2020).

3.2. Observational Data

In this section, we briefly describe the 15 sources used in our work. In Özel et al. (2016), measurements of two different types of sources are reported: the thermonuclear bursters and the qLMXBs.[3] The burst sources are 4U 1820–30, SAX J1748.9–2021, EXO 1745–248, KS 1731–260, 4U 1724–207, and 4U 1608–52. The mass–radius posteriors for these sources are calculated using their apparent angular sizes, touchdown fluxes, and distances. The qLMXBs are M13, M30, NGC 6304, NGC 6397, and ω Cen. In quiescence, the heat accumulated in the crusts of the stars during accretion is radiated through a light element atmosphere. The mass–radius posteriors of the qLMXBs are inferred from the spectral analysis of the thermal emission.

Another source of information comes from the X-ray burst cooling tail spectra of the NS in 4U 1702–429, for which Nättilä et al. (2017) derived $M = 1.9 \pm 0.3\ M_\odot$ and $R = 12.4 \pm 0.4$ km. Additionally, the mass and radius of the millisecond pulsar PSR J0030+0451 have been estimated by the NICER collaboration through pulse profile modeling, resulting in $M = 1.34^{+0.15}_{-0.16} M_\odot$, $R = 12.71^{+1.14}_{-1.19}$ km (Riley et al. 2019b). Following Jiang et al. (2020) for both 4U 1702–429 and PSR J0030+0451, we use a bivariate Gaussian distribution to mimic the mass–radius posteriors of these sources:

$$P(M, R) = \frac{1}{2\pi\sigma_M\sigma_R\sqrt{1-\rho^2}} \times \exp\left\{-\frac{1}{2(1-\rho^2)} \times \left[\frac{(M-\mu_M)^2}{\sigma_M^2} - 2\rho\frac{(M-\mu_M)(R-\mu_R)}{\sigma_M\sigma_R} + \frac{(R-\mu_R)^2}{\sigma_R^2}\right]\right\}. \quad (6)$$

For PSR J0030+0451, we use $\mu_M = 1.34\ M_\odot$, $\mu_R = 12.71$ km, $\sigma_M = 0.155\ M_\odot$, $\sigma_R = 1.165$ km, and $\rho = 0.9$. The value of ρ is chosen to mimic the highly correlated behavior of the data (Jiang et al. 2020).

Similarly, for 4U 1702–429, we use $\mu_M = 1.9\ M_\odot$, $\mu_R = 12.4$ km, $\sigma_M = 0.3\ M_\odot$, $\sigma_R = 0.4$ km, and $\rho = 0.9$, as before to represent the correlation between the measurements.

[3] The M–R distributions of the sources of Özel et al. (2016) are available at http://xtreme.as.arizona.edu/neutronstars/.

Table 2
Most Probable Empirical Parameters from the Joint Posterior Along with the Calculated L

Models	m^*	K (MeV)	n_0 (fm^{-3})	S (MeV)	E_0 (MeV)	L (MeV)
Baseline	0.759	204.1	0.160	29.3	−16.32	81.2
Marg_unif	0.710	219.1	0.152	31.3	−16.26	90.9
Marg_Gauss	0.713	163.8	0.150	34.5	−16.23	100.6
Wide_unif	0.760	178.1	0.156	27.0	−16.65	74.7
	0.761	280.2	0.173	19.2	−16.43	49.8
Wide_Gauss	0.760	177.6	0.151	37.6	−16.16	106.9
Wide_unif with Λ	0.682	319.8	0.170	17.6	−16.72	50.6
Baseline with Λ	0.704	279.2	0.142	28.7	−16.11	83.2

Note. Additionally, for Wide_unif, the parameters associated with the second mode of the PDF are also listed.

Table 3
$R_{1.4}$ and Maximum Mass of the Most Probable Configuration of the Joint Posterior

Models	Baseline	Marg_unif	Marg_Gauss	Wide_unif	Wide_Gauss	Wide_unif with Λ	Baseline with Λ
$R_{1.4}$ (km)	12.58	13.47	12.55	11.70 | 12.15	12.32	12.80	14.18
$\Delta R_{1.4}$ (km)	12.48–13.30	13.43–13.84	11.82–13.24	11.16–12.78	11.32–13.18	12.71–13.25	14.13–14.24
$M_{\max}$ ($M_\odot$)	2.01	2.29	2.27	2.00 | 2.00	2.03	2.01	2.00
$\Delta M_{\max}$ ($M_\odot$)	2.00–2.24	2.28–2.42	2.11–2.46	2.00–2.39	2.00–2.40	2.00–2.10	2.00–2.03

Note. Ranges of $R_{1.4}$ and maximum mass corresponding to the samples within the 68% CI of the empirical parameters.

Finally, we include the EOS insensitive posterior samples computed by the LVC for the masses and radii of the two components of GW170817 (Abbott et al. 2017, 2018).[4]

While this work was in progress, another BNS merger event, GW190425, was reported by the LVC (Abbott et al. 2020). Since this event was reported to be less constraining of the NS properties, we do not include the data from GW190425 in the present analysis.

4. Simulation Results

We construct the joint PDFs of the nuclear empirical parameters $\{m^*, K, n_0, S, E_0\}$ following the method described in the previous section, assuming the five different priors listed in Table 1 and including the sources in Section 3.2. Then, we calculate the slope parameter of the symmetry energy (L) and the distributions of the RMF coupling constants a posteriori from the samples of the PDF. The parameter values corresponding to the most probable points of the joint PDFs are listed in Table 2. Notice that we are including the calculations with hyperons using the baseline and Wide_unif priors. Hence, we have seven different calculations for the comparative analyses of the priors and the effects of the hyperons. A comment about the values of L is mandatory: the most probable values listed in Table 2 are typically outside the now accepted range for L; see Lattimer & Lim (2013) and Xie & Li (2019). The case of the uniform prior is the one with the smallest values of L, with its second mode providing $L \sim 50$ MeV. Therefore, we retain the results obtained within the uniform prior to be more relevant from a phenomenological point of view. We notice, however, that for what concerns astrophysical observables, such as $R_{1.4}$, they could be related not only to L (Hornick et al. 2018) but also to higher-order terms in the symmetry energy expansion, such as $K_{\rm sym}$ and $J_{\rm sym}$ (Zhang & Li 2019), which are, however, affected by large uncertainties. In particular, $-400\,{\rm MeV} < K_{\rm sym} < 100\,{\rm MeV}$ and $-200\,{\rm MeV} < J_{\rm sym} < 800\,{\rm MeV}$ (Zhang & Li 2019); see Carson et al. (2019) for more recent and tighter constraints. In the Appendix, we show in Figure A8 the density dependence of the symmetry energy for the same EOSs together with the values of these two high-order derivatives. Interestingly, their values are within the uncertainties mentioned above.

We use the python corner.py package to visualize one- and two-dimensional projection plots of the samples (Foreman-Mackey 2016). In the two-dimensional plots, we show the contours at 1σ (39.3%), 68%, and 90% confidence intervals (CIs). Next, we draw the mass–radius sequences corresponding to the samples within the 68% CI of the joint posterior and include the most likely sequences for all of the priors. The maximum mass and $R_{1.4}$ for the most likely sequences, along with the minimum and maximum values of $R_{1.4}$ and $M_{\max}$ calculated from the samples within the 68% CI of the joint posterior, are listed in Table 3. The median values of the marginalized distribution of $R_{1.4}$ are listed in Table 4. It should be noted that the values of the most probable sequence are associated with the most probable set of empirical parameters of the joint posterior. This does not necessarily correspond to the distribution of the radii calculated from those EOSs. For example, several sets of parameters that give equally big radii can shift the histogram of the radii toward larger values. Therefore, even though those combinations are less probable individually, they shift the peak of the radius distribution away from the value corresponding to the most probable set.

[4] The data from GW170817 are available at https://dcc.ligo.org/LIGO-P1800115/public.

Table 4
Median of the Distribution for $R_{1.4}$

Models	Baseline	Marg_unif	Marg_Gauss	Wide_unif	Wide_Gauss	Wide_unif with Λ	Baseline with Λ
$R_{1.4}$ (km)	$12.95^{+0.25}_{-0.20}$	$13.68^{+0.09}_{-0.12}$	$12.56^{+0.37}_{-0.29}$	$12.42^{+0.31}_{-0.33}$	$12.37^{+0.37}_{-0.38}$	$13.00^{+0.22}_{-0.16}$	$14.19^{+0.03}_{-0.03}$

Table 5
Bayes Factors (BF_{01})

Model 1	Model 0						
	Baseline	Marg_unif	Marg_Gauss	Wide_unif	Wide_Gauss	Wide_unif with Λ	Baseline with Λ
Baseline		$4 \cdot 10^{-5}$ n. decisive	0.04 n. strong	6.5 p. moderate	30.2 p. strong	0.03 n. very strong	**$1.4 \cdot 10^{-7}$** **n. decisive**
Marg_unif	$2.4 \cdot 10^{4}$ p. decisive		951.3 p. decisive	$1.6 \cdot 10^{5}$ p. decisive	$7.2 \cdot 10^{5}$ p. decisive	710.4 p. decisive	0.003 n. decisive
Marg_Gauss	25.1 p. strong	0.001 n. decisive		163.7 p. decisive	756.8 p. decisive	0.75 n. weak	$3.6 \cdot 10^{-6}$ n. decisive
Wide_unif	**0.15** **n. moderate**	$6.4 \cdot 10^{-6}$ n. decisive	0.006 n. decisive		4.6 p. moderate	**0.005** **n. decisive**	$2.2 \cdot 10^{-8}$ n. decisive
Wide_Gauss	0.03 n. strong	$1.4 \cdot 10^{-6}$ n. decisive	0.001 n. decisive	**0.21** **n. moderate**		0.001 n. decisive	$4.7 \cdot 10^{-9}$ n. decisive
Wide_unif with Λ	33.6 p. very strong	0.001 n. decisive	1.34 p. weak	219.2 p. decisive	1013.4 p. decisive		$4.8 \cdot 10^{-6}$ n. decisive
Baseline with Λ	$7. \cdot 10^{6}$ p. decisive	293.5 p. decisive	$2.8 \cdot 10^{5}$ p. decisive	$4.6 \cdot 10^{7}$ p. decisive	$2.1 \cdot 10^{8}$ p. decisive	$2.1 \cdot 10^{5}$ p. decisive	

Note. We indicate the strength of the preference between the two compared models. Here p. (n.) suggests a positive (negative) preference for model 0 over model 1. The bold entries indicate the most important quantities of our analysis.

Table 6
ΔBIC_{01}

Model 1	Model 0						
	Baseline	Marg_unif	Marg_Gauss	Wide_unif	Wide_Gauss	Wide_unif with Λ	Baseline with Λ
Baseline		17.72 n. decisive	−1.07 p. weak	−2.11 p. moderate	−2.33 p. moderate	2.49 n. moderate	**24.00** **n. decisive**
Marg_unif	−17.72 p. decisive		−18.79 p. decisive	−19.83 p. decisive	−20.05 p. decisive	−15.24 p. decisive	6.26 n. strong
Marg_Gauss	1.07 n. weak	18.79 n. decisive		−1.04 p. weak	−1.26 p. weak	3.55 n. moderate	25.05 n. decisive
Wide_unif	**2.11** **n. moderate**	19.83 n. decisive	1.04 n. weak		−0.22 p. weak	**4.60** **n. moderate**	26.10 n. decisive
Wide_Gauss	2.33 n. moderate	20.05 n. decisive	1.26 n. weak	**0.22** **n. weak**		4.81 n. moderate	26.31 n. decisive
Wide_unif with Λ	−2.49 p. moderate	15.24 n. decisive	−3.55 p. moderate	−4.60 p. moderate	−4.81 p. moderate		21.50 n. decisive
Baseline with Λ	−24.00 p. decisive	−6.26 p. strong	−25.05 p. decisive	−26.10 p. decisive	−26.31 p. decisive	−21.50 p. decisive	

Note. We indicate the strength of the preference between the two compared models. Here p. (n.) suggests a positive (negative) preference for model 0 over model 1. The bold entries indicate the most important quantities of our analysis.

We calculate the evidence and BIC for each model and compute the BFs as the ratio between evidence. This allows for a quantitative comparison of the best plausible scenario among the ones considered in this study. The values of the BFs and ΔBICs are listed in Tables 5 and 6, respectively. For the sake of clarity, the tables contain all seven cases, but in the main text, only the plots and results for the baseline, Wide_unif, and Wide_Gauss priors and the baseline prior with Λ are presented. We refer to the Appendix for the details of the calculations and the results obtained for the Marg_unif and Marg_Gauss priors and Wide_unif prior with Λ.

In Figure 1, we present the marginalized PDFs for the empirical parameters with the baseline prior (the corresponding RMF

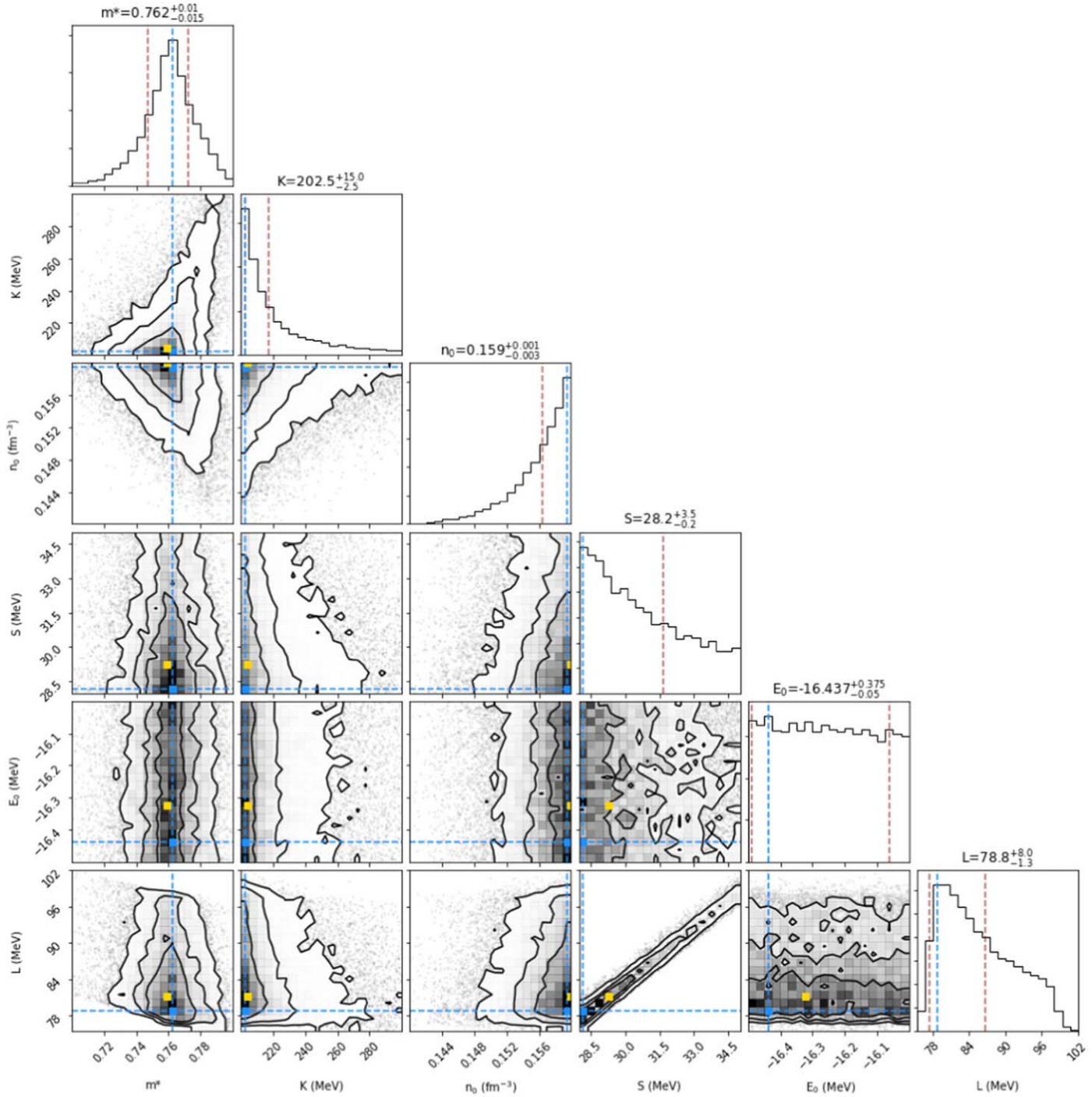

Figure 1. Posterior distributions of the empirical parameters for the baseline prior. In the marginalized one-dimensional plots, the blue lines correspond to the mode and the maroon lines the 1σ CI. The contours in the two-dimensional PDFs are at 1σ (39.3%), 68%, and 90% CIs. The yellow points represent the most probable values for the joint posterior.

coupling constants are shown in Figure A1 in the Appendix). The most probable parameters of the joint PDF are shown as the yellow points in the marginalized plots. We see a prominent peak for m^* and a flat distribution in E_0, while K, n_0, and S show a trend of having the most probable configurations at the edge of the prior boundaries. The peak of m^* can be understood by considering its strong correlation with the maximum mass (Weissenborn et al. 2012b): the smaller the value of m^*, the larger the value of the maximum mass. Since at the same time, the sources point toward not-too-large radii, m^* prefers values that are not too small. For what concerns K, n_0, and S, they affect the stiffness of the EOS at not-too-high densities; therefore, their values are mostly constrained by the radii of the sources. This can be understood more clearly from the inferred mass–radius curves plotted in Figure 2. The most probable sequence lies on the edge of the 68% CI of the inferred EOSs. It is also compatible at the 68% CI for most of the sources. Only ω Cen shows a mild tension with the most probable sequence.

In Figure 3, we present the result for the empirical parameters with the Wide_unif prior. The m^* is peaked at a

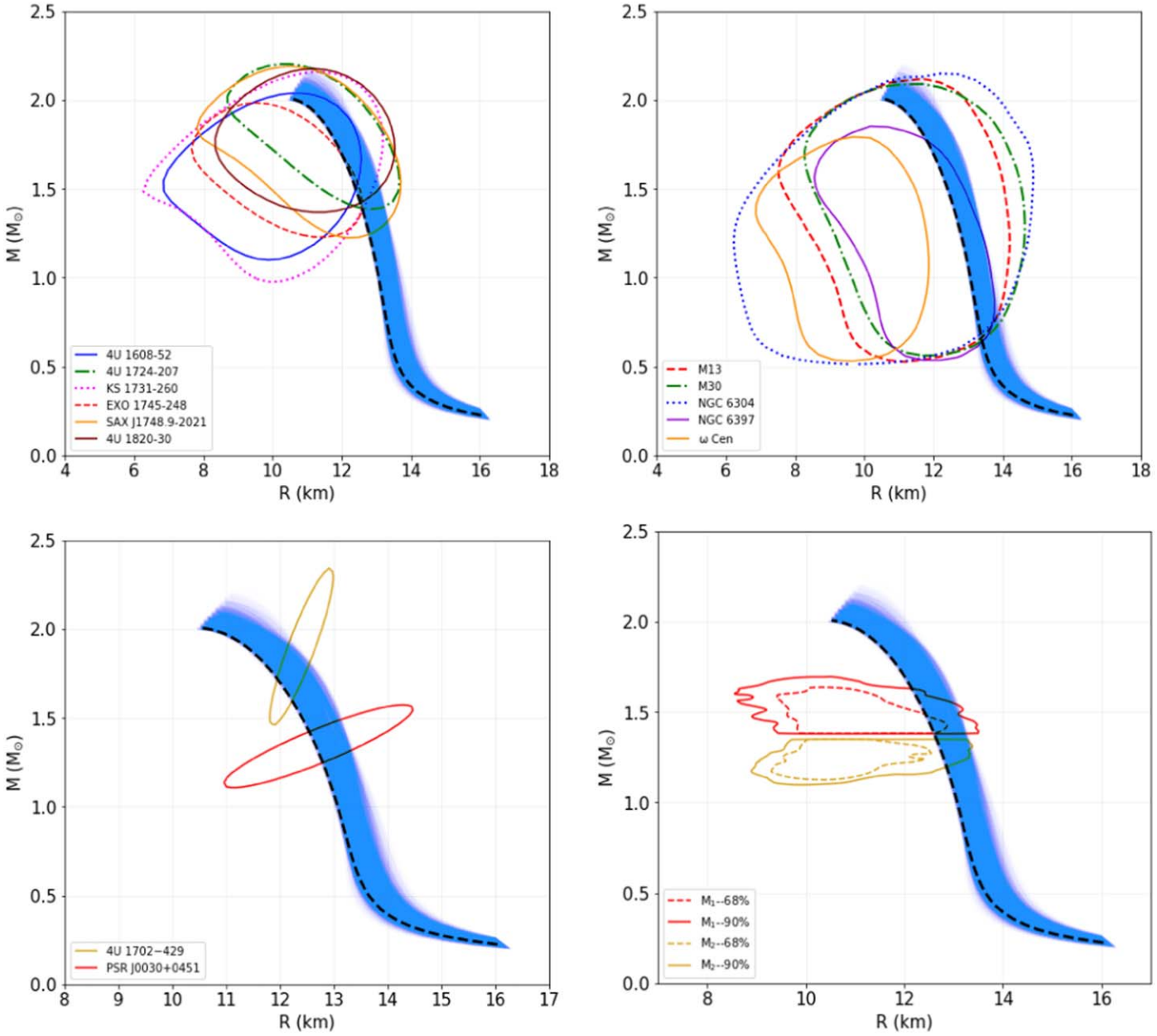

Figure 2. Inferred mass–radius curves corresponding to the EOS parameters up to the 68% CI, assuming the baseline prior along with the sources. The bottom right panel corresponds to the event GW170817. The black dashed lines in all panels represent the most probable EOS parameter set.

slightly different value than the baseline prior. The other parameters, K, n_0, and S, also follow a similar trend, with the most probable values at the edges of the parameter space. In the joint posterior, we find a hint of bimodality that is not evident in the marginalized PDFs. In Figure 3, we indicate the values corresponding to the two modes with yellow (absolute maximum) and blue (second relative maximum) points. From Table 2, we see that the value of S for the second maximum is most likely ruled out by presently available nuclear physics analysis. On the other hand, the most probable parameter set is strikingly similar to that of the LS180 supernova EOS, whose values for the empirical parameters are $K = 180$ MeV, $n_0 = 0.155$ fm^{-3}, $S = 28.6$ MeV, and $L = 73.8$ MeV (Lattimer & Swesty 1991). It is remarkable that an RMF model can reproduce the same results obtained within a medium-dependent liquid-drop model.

Concerning the M–R sequences in Figure 4, they also feature a bimodal behavior resulting from the joint PDF. One can see two different regions in the M–R plots where the sequences are clubbed together. The dashed and dotted lines correspond to the two modes, respectively, and show a good agreement with the astrophysical data. However the dotted line is most likely ruled out, as explained before.[5] Interestingly, the most probable sequence shows a bump close to $\sim 1\ M_\odot$, and, contrary to LS180, it reaches the $2\ M_\odot$ limit and its $R_{1.4} = 11.7$ km, thus 0.5 km smaller than the LS180 value. While the saturation properties of these two EOSs are very similar, they show

[5] Notice that this M–R curve is quite similar to the result of the APR EOS (Akmal et al. 1998), which is, however, perfectly compatible with the present knowledge of nuclear symmetry energy. Again, introducing in our Lagrangian other terms aiming at a better description of symmetry energy would possibly lead to solutions like the dashed line that are consistent with nuclear physics and astrophysical data.

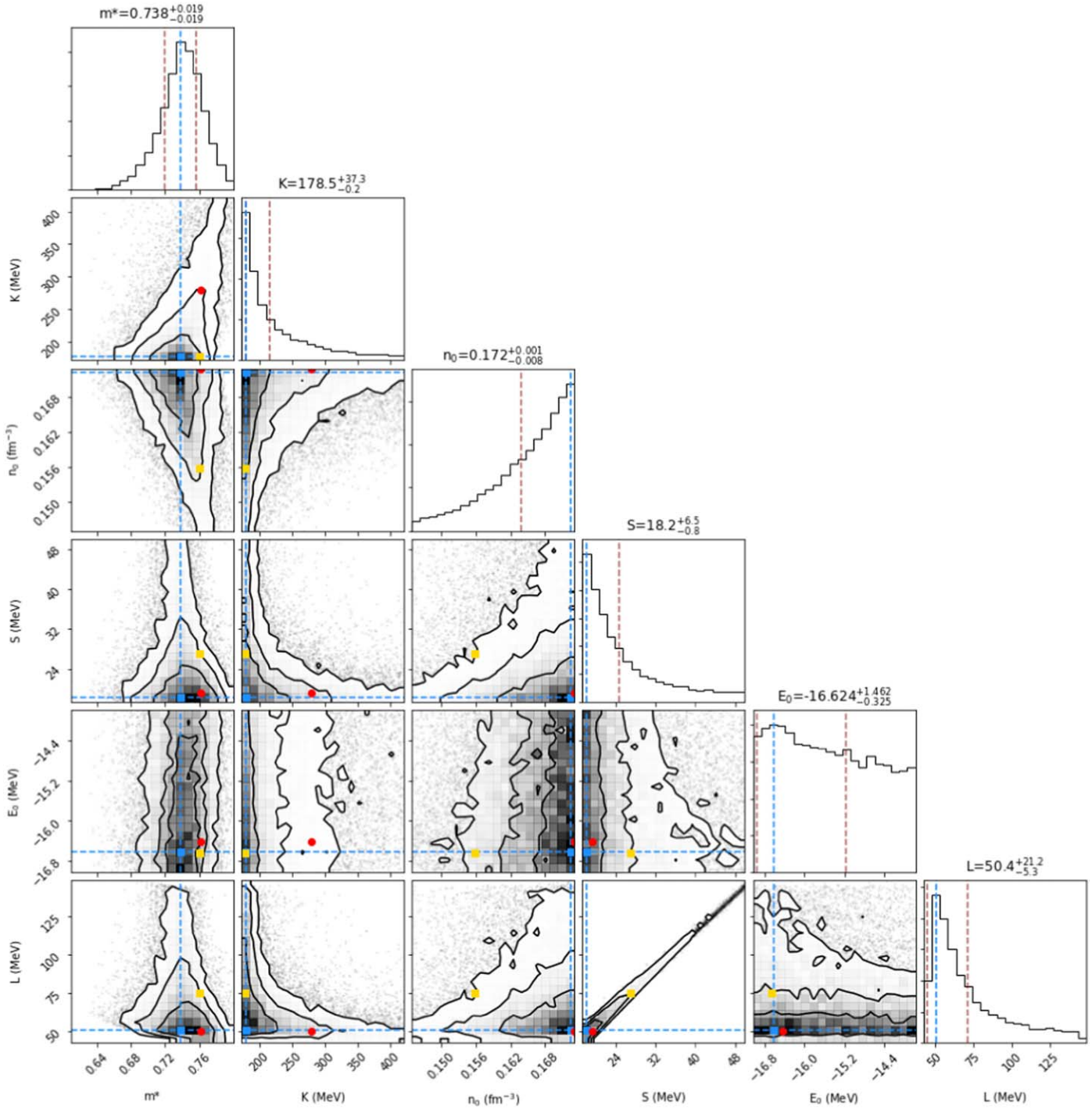

Figure 3. Same as Figure 1 but for the Wide_unif prior. The red points indicate the second mode of the joint distribution.

different high-density behavior for β-stable matter. This can be interpreted as the outcome of the nonlinearity of the RMF parameterization, which will be discussed in the next section.

In Figure 5, the results for the Wide_Gauss prior are shown. Apart from K, the posteriors for the other parameters do not deviate much from the prior distribution. We see a significant shift for the peak of K, which moves about 2σ below the peak of the prior. It implies that the EOS prefers to be rather soft at saturation but stiffer at the higher density due to the high symmetry energy and not-too-high effective mass. A small value of K would be consistent with the analysis of the KaoS collaboration on heavy ion collisions (Sagert et al. 2012). The effect of using a Gaussian prior is to remove the bimodality found in the previous case, but the bump associated with the mass–radius curve of the most probable EOS is still present, as can be seen in Figure 6. The value of $R_{1.4}$ is again smaller than the value obtained with the baseline prior. The correlation between K and the radii has also been noted in Ferreira & Providência (2019).

Next, we investigate the effect of the formation of Λ hyperons in the system. As expected, the appearance of a new degree of freedom softens the EOS. Therefore, most parts of

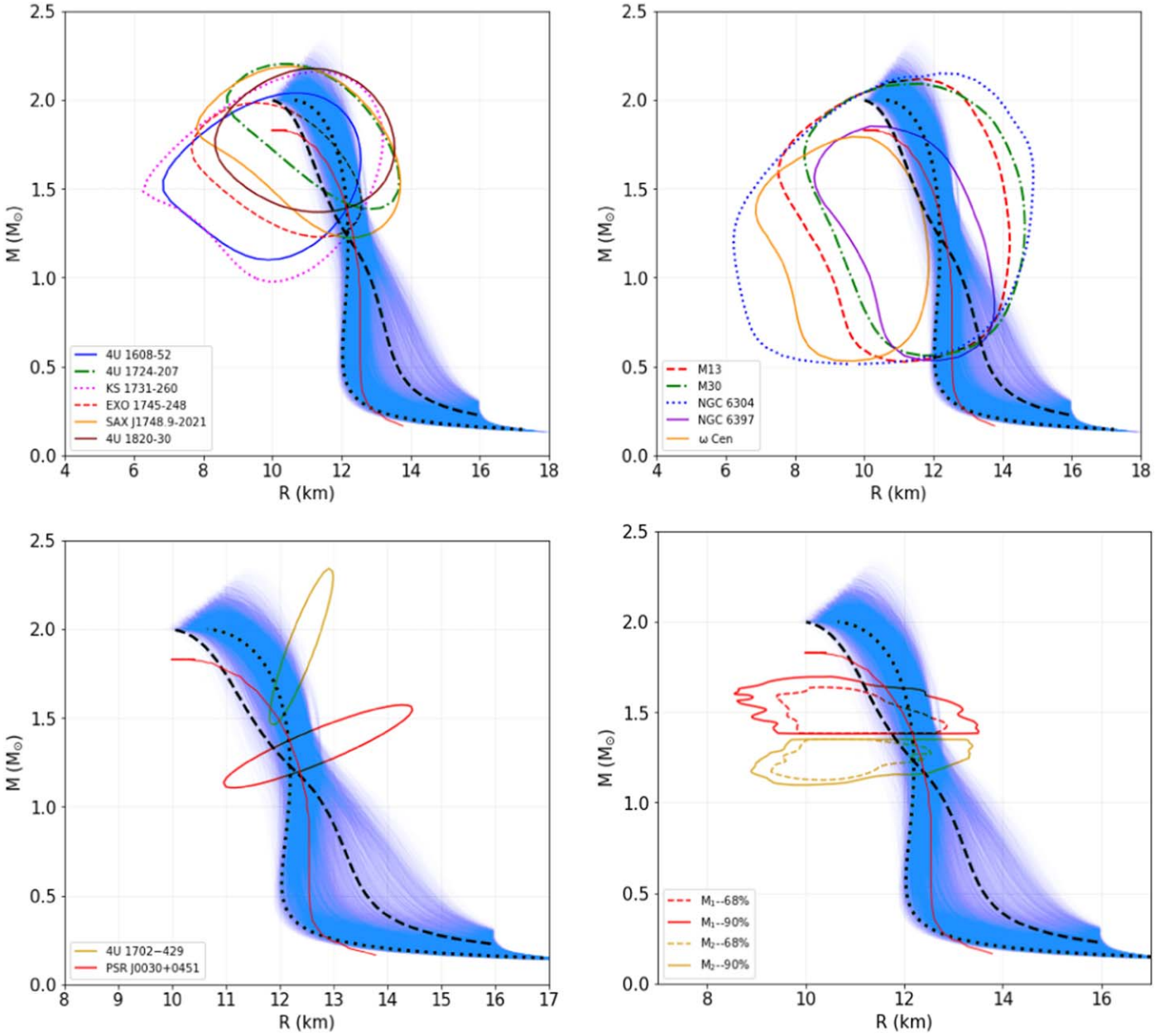

Figure 4. Same as Figure 2 but for the Wide_unif prior. Here the black dotted lines in all panels represent the curve related to the second mode of the joint distribution for the empirical parameters. The red curve shows LS180 for comparison.

the parameter space are not consistent with the 2 $M_{\odot}$ limit and are ruled out. This restricts the parameter space severely. The posteriors for the empirical parameters with the baseline prior and the corresponding M–R sequences are shown in Figures 7 and 8, respectively. The qualitative differences with respect to the previous cases are evident in the marginalized PDF of m^{*} and K. In particular, m^{*} does not exhibit a peak, and its distribution tends toward the lower edge of the range, whereas K prefers the higher edge, contrary to the previous cases. These behaviors arise to compensate for the softening associated with the hyperons in order to fulfill the 2 $M_{\odot}$ criterion. We get M–R sequences that are outside the 68% regions of the posteriors of most of the sources. The value of $R_{1.4}$ for the most probable EOS is more than 14 km, significantly larger than the other cases. In the case of the Wide_unif prior, we find some sequences within the observable limits, but the symmetry energy turns out to be very small, well outside the acceptable region (see Figures A6 and A7 in the Appendix).

Finally, we compare our models using BIC and evidence calculations. From Table 5, we find the highest evidence for the Wide_Gauss prior and the lowest for the Marg_unif prior for the nucleonic models. Between the hyperonic models, the Wide_unif is preferred over the baseline prior. In general, nucleonic models are preferred over hyperonic models. One can draw the same conclusion from the calculations of ΔBIC in Table 6, the only exception being the Marg_Gauss case. The calculation of BIC includes only the likelihood for the most probable configuration and the number of prior parameters. Instead, the BF takes into account the full prior distribution. Therefore, in the case of Gaussian priors, the probabilities away from the central value are suppressed. So, two different models with parameters producing similar maximum-likelihood values

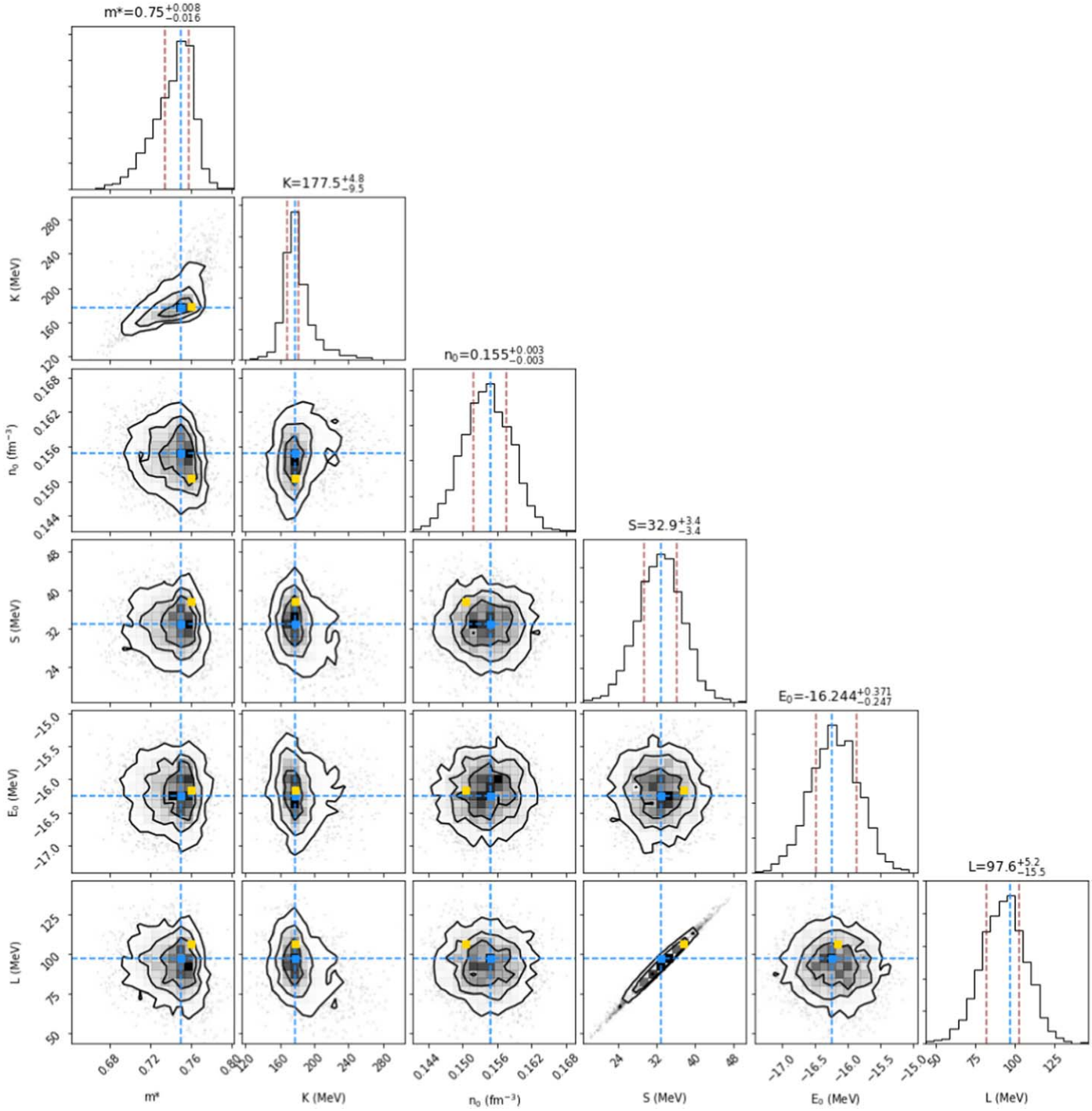

Figure 5. Same as Figure 1 but for the Wide_Gauss prior.

can have similar BICs but different BFs if the nature of the prior distribution is different. This case is realized in the Marg_Gauss prior, as the peak of the posterior for K deviates by more than 3σ with regard to the peak of the prior.

Now, let us focus on the interpretation of the BFs between the two categories of priors: the informed and the agnostic. For the informed prior, we take the baseline model, and for the agnostic, we take the Wide_unif model, for example. If the maximum-likelihood points for both of the models happen to be inside the overlap region of the priors, one would expect the evidence for the Wide_unif to be smaller. This is due to its larger prior volume penalizing it over the baseline prior. The fact that the Wide_unif has more evidence instead suggests a tension between the nuclear physics informed priors and the astrophysical data, consistent with the findings of Güven et al. (2020).

5. Discussion and Conclusions

We have shown before that when considering the uniform informed priors, the M–R relations are qualitatively very similar to the old parameterization of Glendenning & Moszkowski (1991). This result leads to the following conclusion: within the present uncertainties on the nuclear physics empirical parameters and by

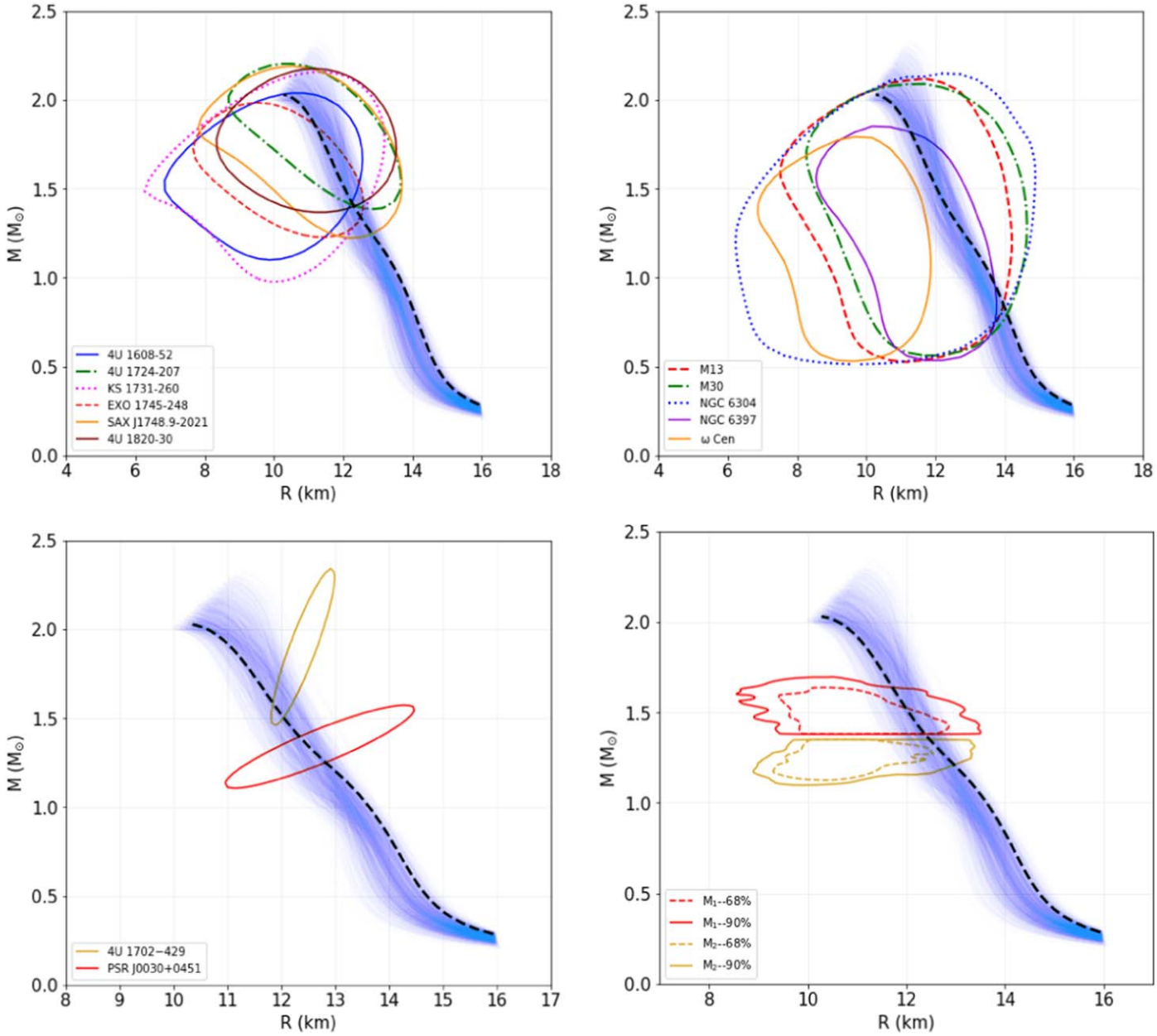

Figure 6. Same as Figure 2 but for the Wide_Gauss prior.

using uniform priors, it is basically impossible to obtain $R_{1.4}$ smaller than ∼12.5 km; see Tables 3 and 4 and Figure 2. Radii close to ∼11 km can be reached only for configurations close to the maximum mass. This conclusion is clearly based on our modeling of the EOS and specifically on our choice of RMF model. However, we would like to remark that this outcome is fully in agreement with the results of the metamodeling analysis of Margueron et al. (2018b) and the independent analysis by Most et al. (2018). In both of those papers, the EOS is modeled in a different way: a Taylor expansion around saturation in the first case, and a chiral effective field theory up to densities close to saturation and a piecewise polytropic parameterization for larger densities. On the other hand, the fact that the most probable *M–R* curve sits on the left border of the 68% CI in both cases is somehow suggesting that there is some tension between the values of the nuclear physics empirical parameters and the astrophysical measurements, as stressed before. That is the main reason for investigating different kinds of priors.

Quite remarkably, when allowing for a wider exploration of the parameters (Wide_unif, Wide_Gauss, and Marg_Gauss; see the Appendix), we see a qualitative difference in the *M–R* relation with a bump appearing at about 1 $M_{\odot}$. That behavior is very similar to the one obtained when a smooth phase transition occurs (for instance, a Gibbs mixed phase with quark matter). To understand the origin of this behavior, one has to check the density dependence of the effective mass (displayed in Figure 9), which, due to the nonlinearity of the sigma potential, could feature a phase transition. Indeed, m^* features a fast drop for the last three priors at densities of two to three times saturation density. Moreover, a change in concavity with respect to the first two priors can also be noticed. This bump is also clearly visible in the plot showing the gravitational mass as

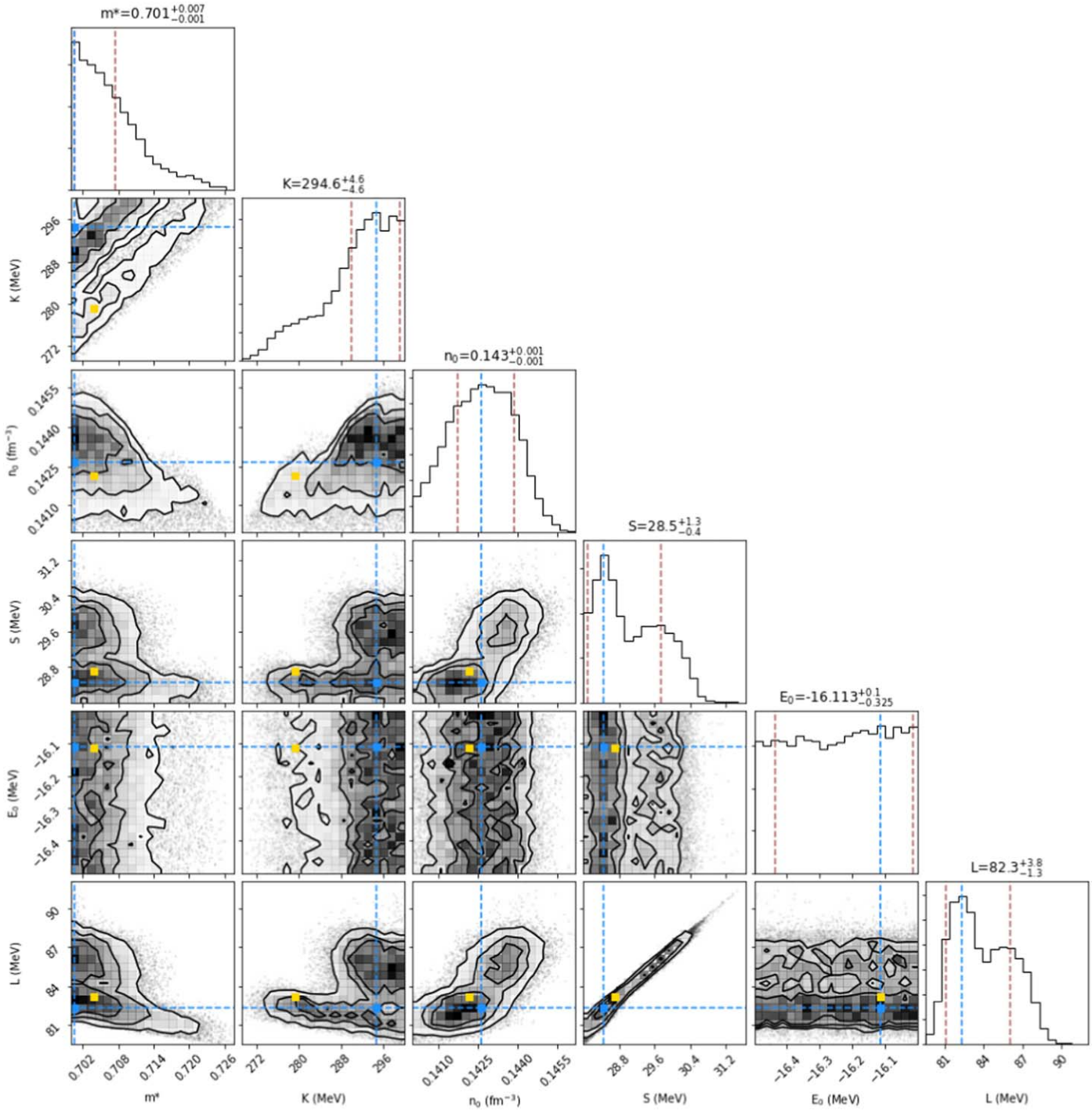

Figure 7. Same as Figure 1 but for the baseline prior with Λ in the system.

a function of the central baryon density; see Figure 10. Such a behavior is reminiscent of a partial restoration of chiral symmetry, and we interpret it as a clear indication that astrophysical measurements are in fact suggesting the appearance of new phases of strongly interacting matter in NSs. Notice that the prior with the largest evidence is the one adopting wide Gaussian distributions for the nuclear empirical parameters; in this case, $R_{1.4}$ could drop below $\sim$12 km, and radii as small as $\sim$10 km are reached at the maximum mass configuration (see Figure 6).

Similar conclusions have been drawn in other works employing different methods; in Essick et al. (2020), Güven et al. (2020), and Fujimoto et al. (2020), hints of a phase transition have been suggested by using the nonparametric inference, metamodeling tools, and deep neural network methods. Previously, a Bayesian analysis with a tuned parameterization of a strong phase transition has led to the very same conclusion (Steiner et al. 2018).

Let us now discuss the cases in which hyperons have been included in the EOS. In Figure 10, we display the relation

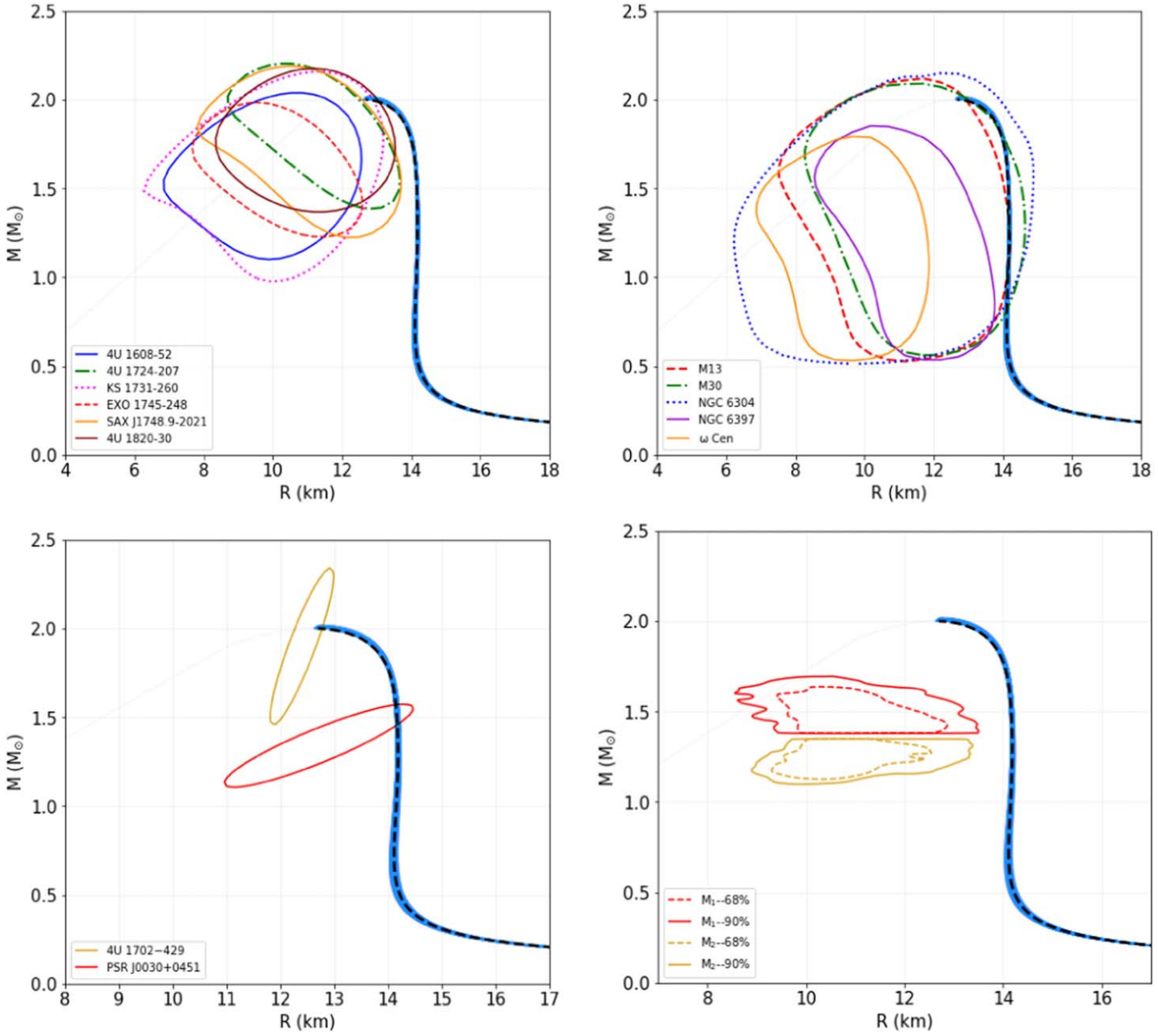

Figure 8. Same as Figure 2 but for the baseline prior range with Λ hyperon in the system.

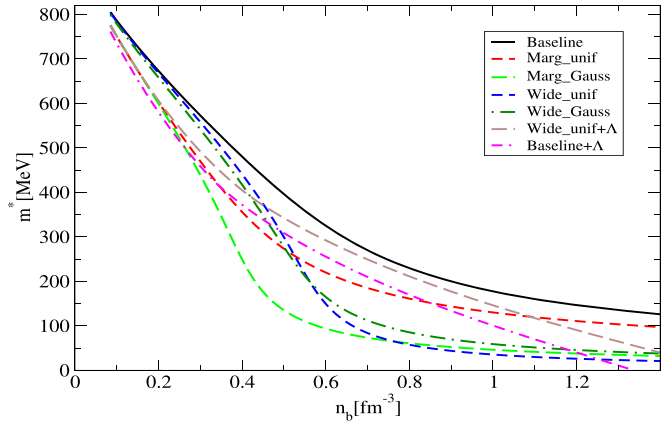

Figure 9. Effective mass as a function of density for the five priors adopted here. The curves correspond to the most probable parameters for each prior. Also, the two cases with the inclusion of Λ are shown.

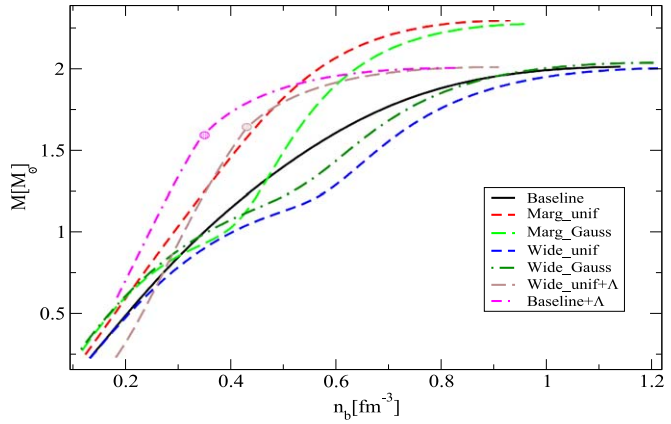

Figure 10. Gravitational mass as a function of central density as obtained from the same EOSs as Figure 9. The circles correspond to the onset of Λ in the EOSs.

between gravitational mass and central density for the different models. In all cases in which hyperons are not included, the central density for the 2 $M_\odot$ configuration is larger than about $4n_0$. Therefore, to justify the approximation of neglecting hyperons in those EOSs, one has to resort to some stiffening mechanism that shifts the threshold of the appearance of hyperons to a larger density, e.g., a strong repulsion due to three-body interactions (Lonardoni et al. 2015) or a hidden strangeness vector field as the ϕ meson; see Weissenborn et al. (2012a). On the other hand, when allowing for the formation of hyperons (only Λ and with fixed couplings in this work), Λ does appear in compact stars with masses larger than about 1.6 $M_\odot$ and up to 2 $M_\odot$. For the Wide_unif case, the possibility of forming hyperons and, at the same time, fulfilling the 2 $M_\odot$ limit is due to an unreasonably small value (both the most probable and the median) of the symmetry energy (see Tables 2 and A1) and a very large value of K. We consider this EOS to be very unlikely. By introducing Λ with the baseline prior, the need to reach 2 $M_\odot$ causes an early stiffening of the EOS such that $R_{1.4} \gtrsim 14$ km. This result is in agreement with previous findings presented in Fortin et al. (2015), where it was suggested that the presence of hyperons systematically shifts the radii of compact stars to larger value with respect to nucleonic stars. As one can notice in Figure 8, the predicted mass–radius curve is outside even the 90% CI provided by GW170817. It is clear that our minimal modeling for including hyperons strengthens the tension between the values of the nuclear physics empirical parameters and the astrophysical measurements. This statement is supported by the results on the BFs.

We plan to further investigate this issue in the future by, for instance, adding a repulsive channel for hyperons. Indeed, there are many examples in the literature in which hyperons do not forbid obtaining values of $R_{1.4}$ close to 12.5–13 km while fulfilling the 2 $M_\odot$ limit; see, e.g., Logoteta et al. (2019) for a recent microscopic calculation and Weissenborn et al. (2012a), Maslov et al. (2015), and Negreiros et al. (2018) for RMF examples. Also, delta resonances should be included in principle, since, as shown in many papers, their onset is actually comparable to that of hyperons (Drago et al. 2014b; Cai et al. 2015; Li et al. 2018). The indications of a possible phase transition found in this paper should also be investigated thoroughly by considering a transition to quark matter via a Gibbs construction; see Weissenborn et al. (2011) and Nandi & Char (2018).

A final possibility is to implement EOSs leading to mass–radius relations with disconnected branches, such as in the twin stars (Benic et al. 2015; Christian et al. 2018) or two families scenarios, in which hadronic and quark stars coexist (Drago et al. 2014a, 2016; Burgio et al. 2018; De Pietri et al. 2019). Interestingly, a very recent analysis of short gamma-ray bursts has provided hints in favor of quark stars being the remnants of the mergers of two compact stars (Sarin et al. 2020).

We would like to thank Alessandro Drago and Pietro Bergamini for useful discussions. P.C. also acknowledges financial support from INFN as a postdoctoral fellow.

Appendix

In this appendix, we provide further calculations for Marg_unif and Marg_Gauss priors and the Wide_unif with Λ. We also present the results for RMF coupling constants for all cases: in Table A2, the most probable values of the joint PDF are listed, while Figure A1 and the corresponding figure set (in the online journal) display their marginalized PDFs. In Table A1, we provide the median values of the marginalized distributions of the empirical parameters.

In Figure A2, we show the results for the Marg_unif prior. Within this particular range, one can usually construct EOSs that are stiffer with respect to the ones obtained with the baseline prior. But, to conform with the observational data, the most probable parameter set for this prior again sits on the edge of the boundary where one can get the softest possible EOS. Compared to the baseline, the difference we get is in the marginalized distribution of m^*, which does not have a peak for the Marg_unif case. Rather, it shows the trend of having the most probable configuration near the edge of the upper limit corresponding to the softest EOS. Otherwise, the trends for K, n_0, and S are similar to those of our baseline prior. In Figure A3, the inferred M–R sequences are shown along with the most probable one. Due to our choice of parameter ranges, the inferred EOSs are stiffer and the M–R sequences are outside of the 68% regions of most of the X-ray sources and the GW data.

In Figure A4, the distribution of the empirical parameters is shown for the Marg_Gauss prior. The peak of K is shifted by more than 3σ from the peak of the prior. The corresponding mass–radius relations shown in Figure A5 are qualitatively similar to Wide_Gauss prior. But the maximum mass for the most probable configuration is much higher, as the EOS becomes stiffer due to fact that the value of m^* is peaked at a much lower value.

The posterior distributions for the Wide_unif with Λ case are shown in Figure A6 and the mass–radius sequences in Figure A7. The preferred K value is very high to reduce the softening of the EOS due to the appearance of hyperons, and the S is very small to make the matter more symmetric, i.e., less neutron-rich, which, in turn, suppresses the production of Λ. But such small values of S are ruled out by the present experimental knowledge. Finally, in Figure A8, we have plotted the density dependence of the symmetry energy for all the priors of Table 1 with the nucleonic EOSs.

Table A1
Median of the Marginalized Distributions for the Empirical Parameters

Models	m^*	K (MeV)	n_0 (fm^{-3})	S (MeV)	E_0 (MeV)	L (MeV)
Baseline	$0.761^{+0.015}_{-0.016}$	$212.7^{+32.0}_{-9.8}$	$0.157^{+0.002}_{-0.004}$	$30.3^{+2.7}_{-1.7}$	$-16.26^{+0.17}_{-0.17}$	$84.4^{+8.3}_{-5.1}$
Marg_unif	$0.705^{+0.004}_{-0.008}$	$226.6^{+13.0}_{-5.7}$	$0.152^{+0.001}_{-0.002}$	$33.4^{+3.0}_{-1.7}$	$-16.24^{+0.08}_{-0.08}$	$97.6^{+8.8}_{-5.0}$
Marg_Gauss	$0.707^{+0.016}_{-0.014}$	$161.1^{+14.0}_{-11.9}$	$0.151^{+0.002}_{-0.002}$	$34.7^{+2.9}_{-2.7}$	$-16.24^{+0.06}_{-0.06}$	$101.7^{+8.6}_{-8.1}$
Wide_unif	$0.740^{+0.023}_{-0.027}$	$203.5^{+82.7}_{-24.9}$	$0.166^{+0.005}_{-0.009}$	$22.7^{+11.7}_{-4.1}$	$-15.57^{+1.17}_{-1.02}$	$62.7^{+35.3}_{-12.4}$
Wide_Gauss	$0.746^{+0.014}_{-0.024}$	$177.3^{+18.1}_{-10.9}$	$0.154^{+0.004}_{-0.004}$	$32.8^{+4.5}_{-4.8}$	$-16.20^{+0.37}_{-0.37}$	$93.3^{+13.6}_{-14.1}$
Wide_unif with Λ	$0.683^{+0.024}_{-0.029}$	$355.9^{+44.0}_{-58.7}$	$0.169^{+0.003}_{-0.006}$	$18.9^{+2.5}_{-1.0}$	$-15.40^{+1.09}_{-1.14}$	$54.9^{+8.7}_{-4.9}$
Baseline with Λ	$0.706^{+0.006}_{-0.004}$	$292.1^{+5.4}_{-9.1}$	$0.143^{+0.001}_{-0.001}$	$28.9^{+1.0}_{-0.6}$	$-16.24^{+0.17}_{-0.18}$	$83.6^{+3.0}_{-2.0}$

Table A2
Most Probable RMF Coupling Constants from the Joint PDF

Models	g_σ/m_σ (fm)	g_ω/m_ω (fm)	g_ρ/m_ρ (fm)	b	c
Baseline	3.252	2.270	1.888	0.00991	−0.01083
Marg_unif	3.505	2.629	2.047	0.00548	−0.00615
Marg_Gauss	3.585	2.628	2.267	0.00713	−0.00985
Wide_unif	3.351	2.296	1.774	0.01148	−0.01510
	3.000	2.153	0.882	0.00596	0.00231
Wide_Gauss	3.381	2.351	2.490	0.01056	−0.01373
Wide_unif with Λ	3.340	2.609	0.274	0.00279	−0.00129
Baseline with Λ	3.556	2.768	1.971	0.00319	−0.00180

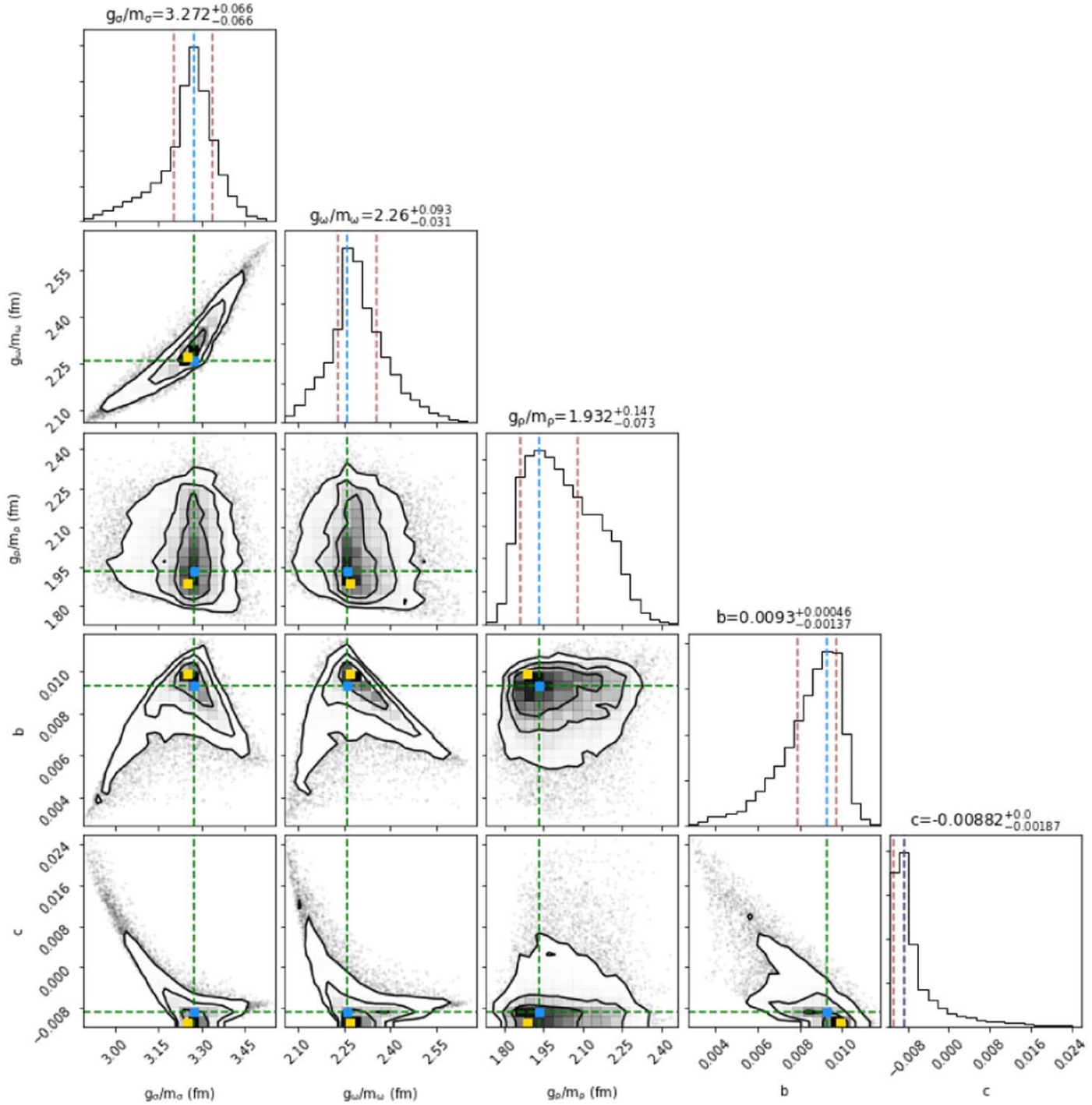

Figure A1. Distribution of RMF parameters corresponding to the empirical parameters of Figure 1. The complete figure set (six images for the other six priors) is available in the online journal.

(The complete figure set (6 images) is available.)

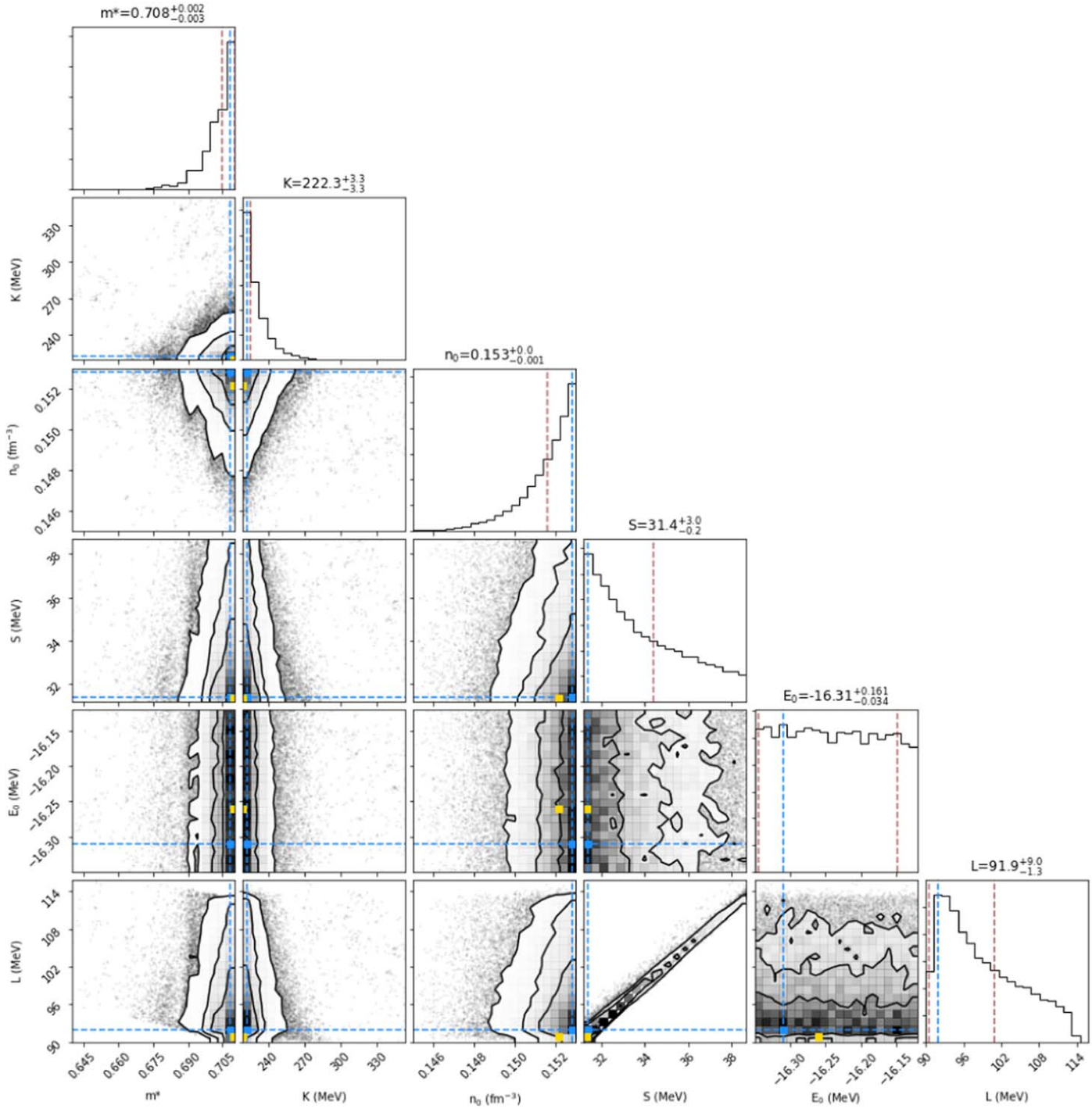

Figure A2. Same as Figure 1 but for the Marg_unif prior.

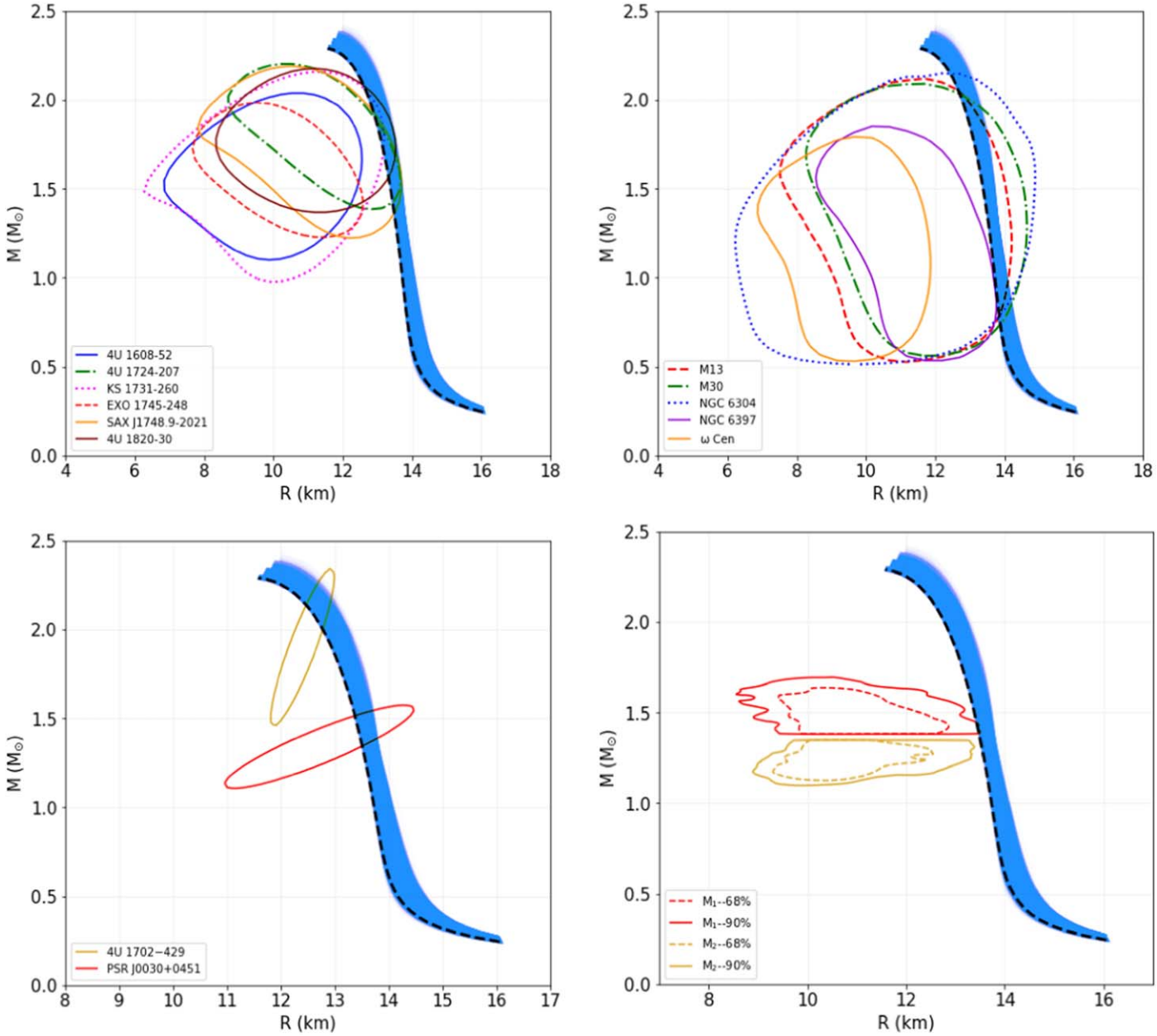

Figure A3. Same as Figure 2 but for the Marg_unif prior.

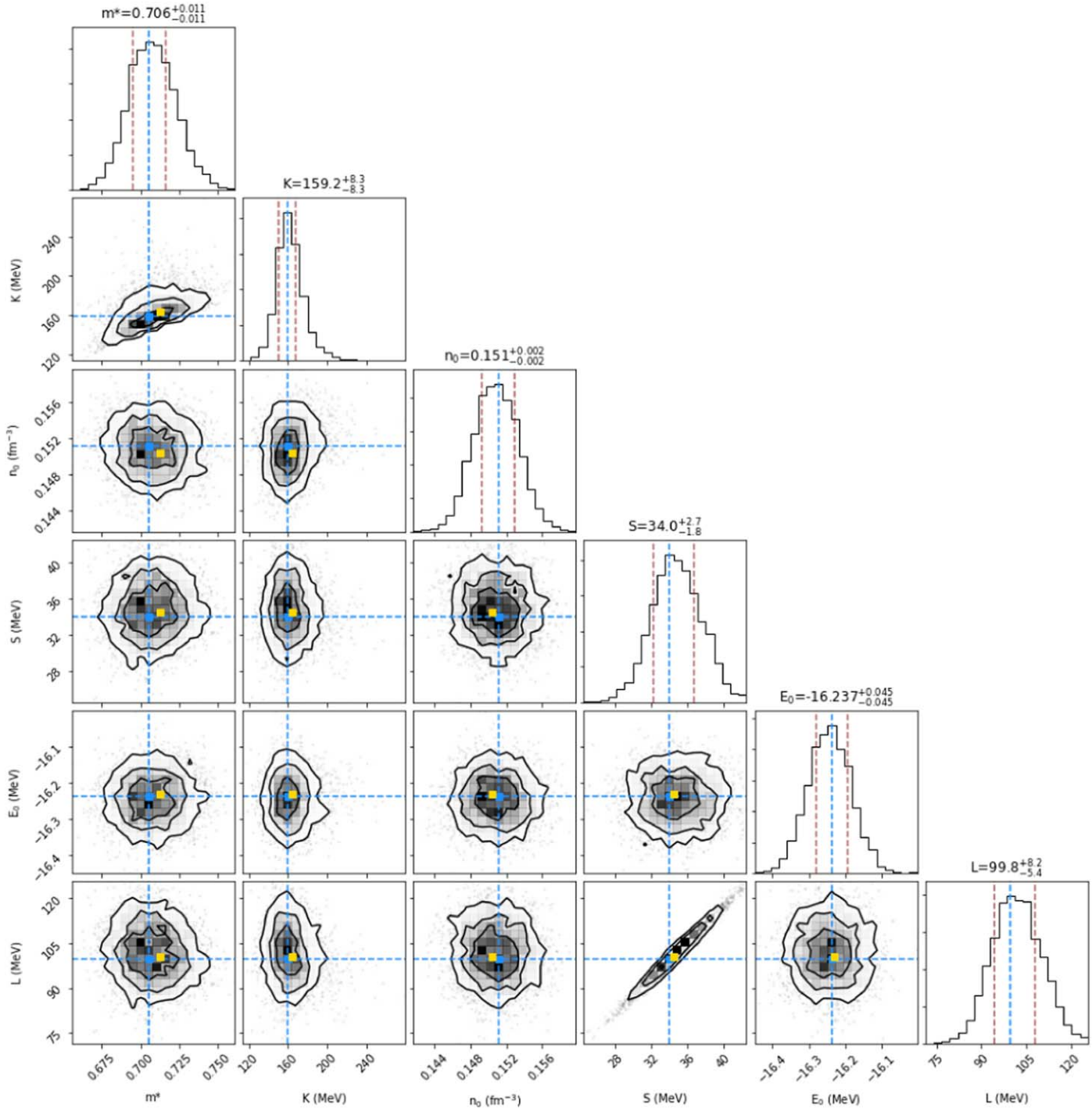

Figure A4. Same as Figure 1 but for the Marg_Gauss prior.

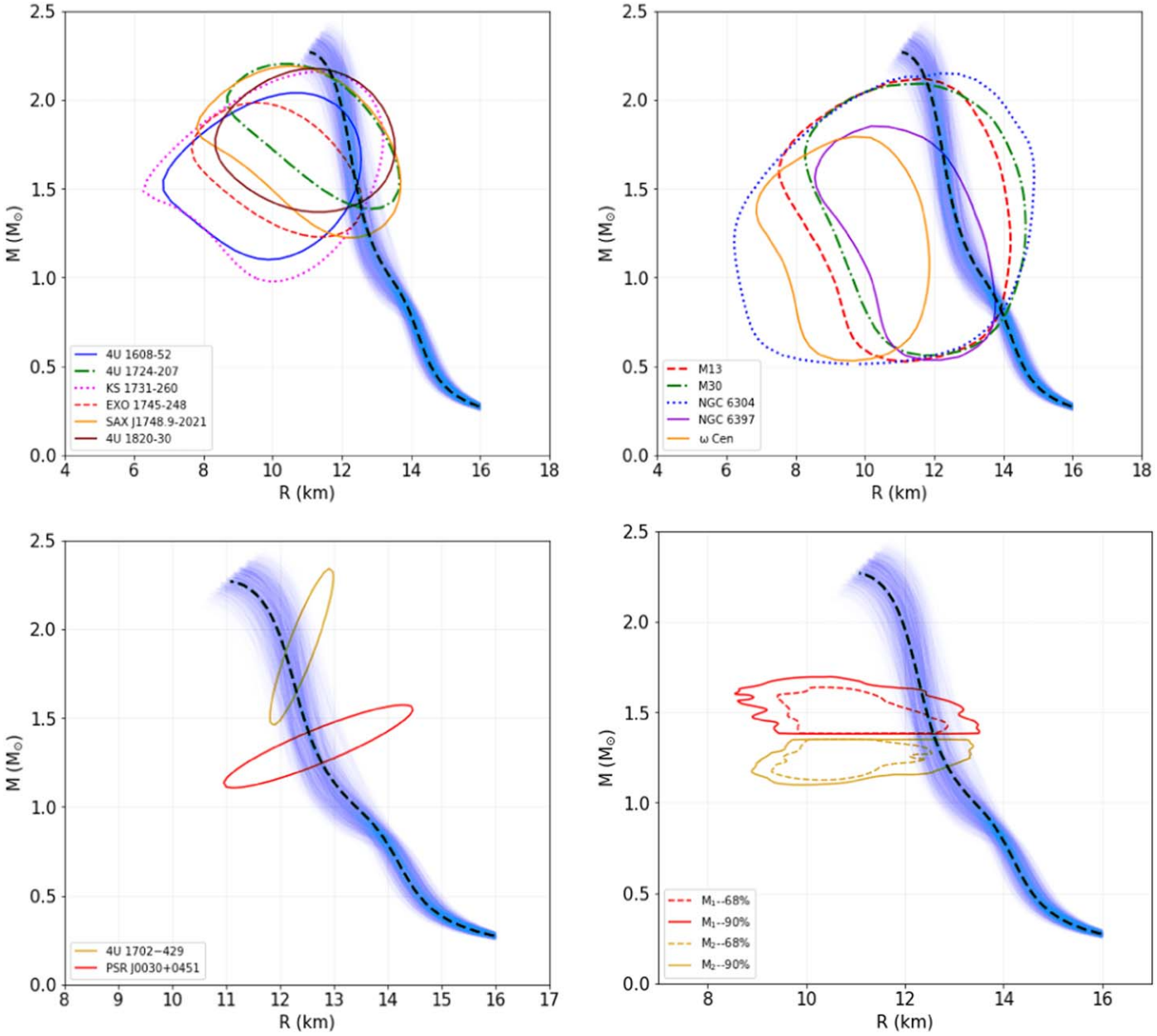

Figure A5. Same as Figure 2 but for the Marg_Gauss prior.

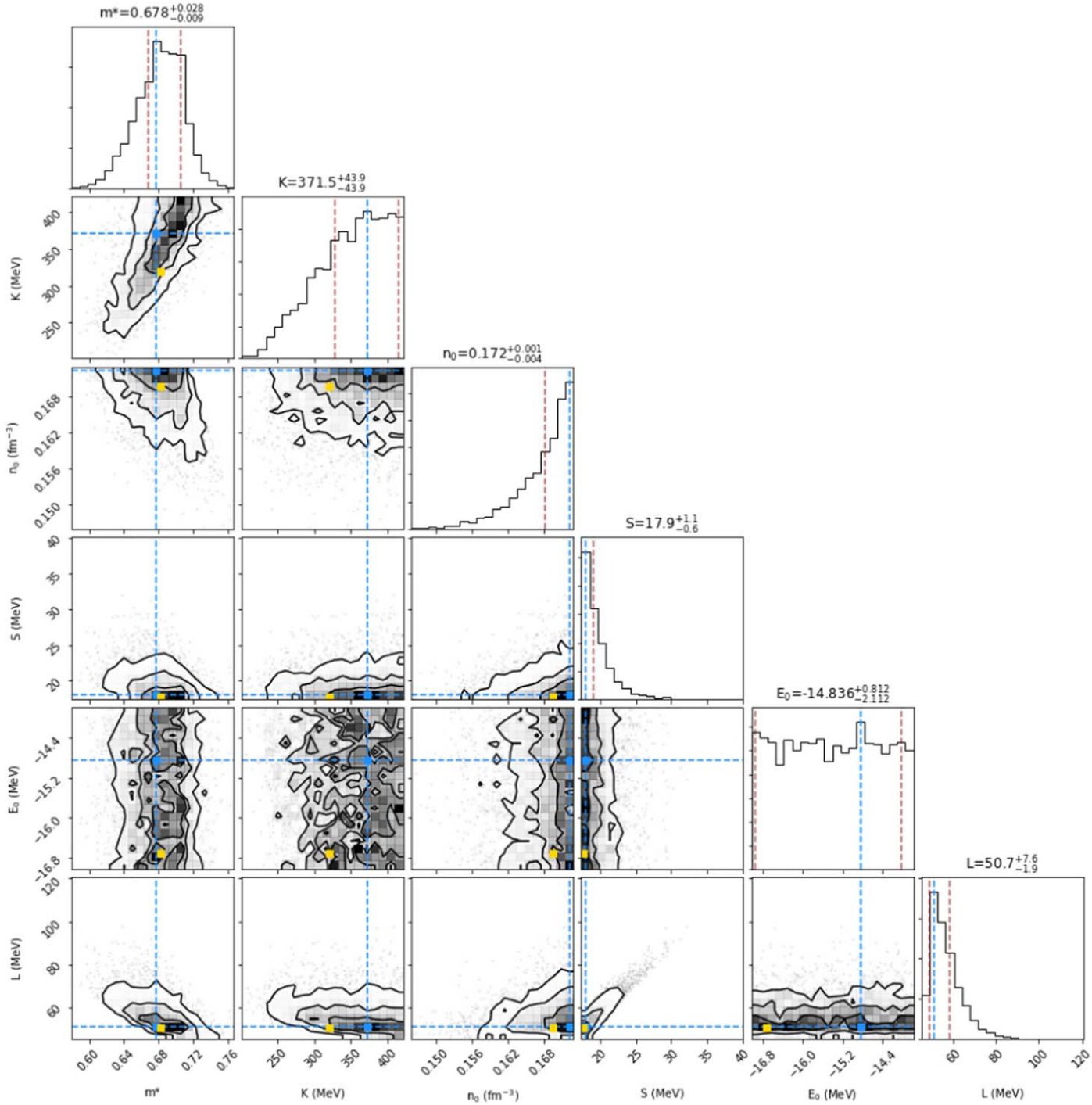

Figure A6. Same as Figure 1 but for the Wide_unif with Λ in the system.

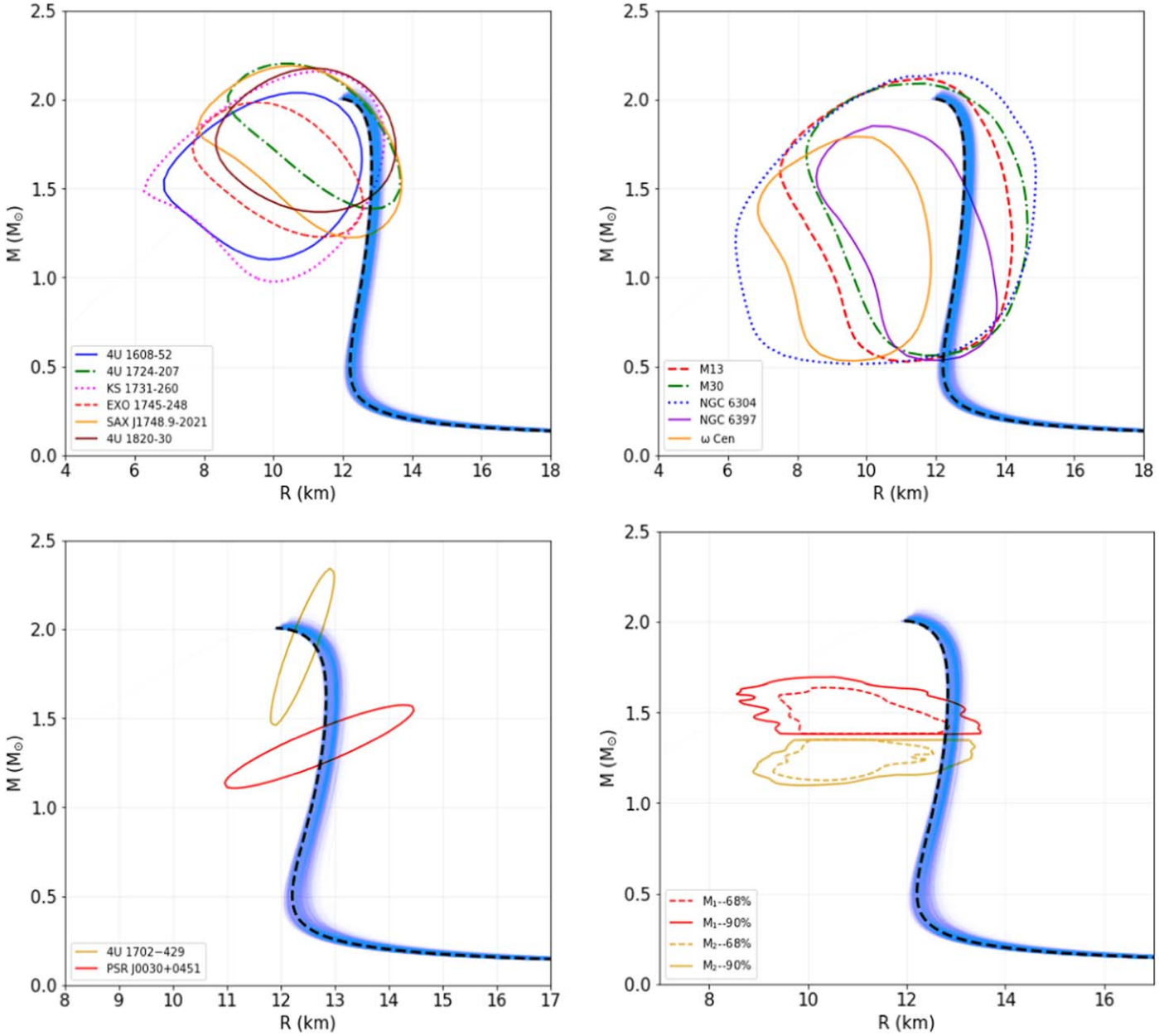

Figure A7. Same as Figure 2 but for the Wide_unif with Λ in the system.

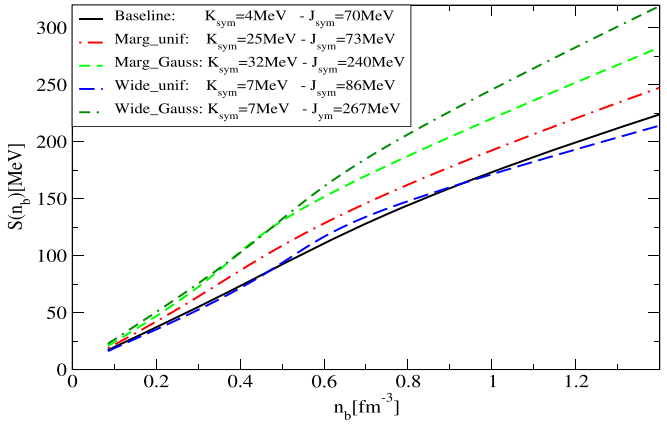

Figure A8. Density dependence of symmetry energy for the same EOS of Figure 9. We also indicate the high-order derivatives $K_{\rm sym}$ and $J_{\rm sym}$.

ORCID iDs

Silvia Traversi https://orcid.org/0000-0002-8410-520X
Prasanta Char https://orcid.org/0000-0001-6592-6590
Giuseppe Pagliara https://orcid.org/0000-0003-3250-1398

References

Abbott, B. P., Abbott, R., Abbott, T. D., et al. 2017, PhRvL, 119, 161101
Abbott, B. P., Abbott, R., Abbott, T. D., et al. 2018, PhRvL, 121, 161101
Abbott, B. P., Abbott, R., Abbott, T. D., et al. 2020, ApJ, 892, 3
Akmal, A., Pandharipande, V. R., & Ravenhall, D. G. 1998, PhRvC, 58, 1804
Alvarez-Castillo, D., Ayriyan, A., Benic, S., et al. 2016, EPJA, 52, 69
Antoniadis, J., Freire, P. C. C., Wex, N., et al. 2013, Sci, 340, 448
Arzoumanian, Z., Brazier, A., Burke-Spolaor, S., et al. 2018, ApJS, 235, 37
Banik, S., Hempel, M., & Bandyopadhyay, D. 2014, ApJS, 214, 22
Benic, S., Blaschke, D., Alvarez-Castillo, D. E., Fischer, T., & Typel, S. 2015, A&A, 577, A40
Boguta, J., & Bodmer, A. R. 1977, NucPh, A292, 413
Bonanno, L., & Drago, A. 2009, PhRvC, 79, 045801
Burgio, G. F., Drago, A., Pagliara, G., Schulze, H. J., & Wei, J. B. 2018, ApJ, 860, 139
Cai, B.-J., Fattoyev, F. J., Li, B.-A., & Newton, W. G. 2015, PhRvC, 92, 015802
Capano, C. D., Tews, I., Brown, S. M., et al. 2020, NatAs, 4, 625
Carson, Z., Steiner, A. W., & Yagi, K. 2019, PhRvD, 99, 043010
Christian, J.-E., Zacchi, A., & Schaffner-Bielich, J. 2018, EPJA, 54, 28
Cromartie, H. T., Fonseca, E., Ransom, S. M., et al. 2019, NatAs, 4, 72
De Pietri, R., Drago, A., Feo, A., et al. 2019, ApJ, 881, 122
Demorest, P., Pennucci, T., Ransom, S., Roberts, M., & Hessels, J. 2010, Natur, 467, 1081
Drago, A., Lavagno, A., & Pagliara, G. 2014a, PhRvD, 89, 043014
Drago, A., Lavagno, A., Pagliara, G., & Pigato, D. 2014b, PhRvC, 90, 065809
Drago, A., Lavagno, A., Pagliara, G., & Pigato, D. 2016, EPJA, 52, 40
Dutra, M., Lourenço, O., Avancini, S. S., et al. 2014, PhRvC, 90, 055203
Essick, R., Landry, P., & Holz, D. E. 2020, PhRvD, 101, 063007
Fasano, M., Abdelsalhin, T., Maselli, A., & Ferrari, V. 2019, PhRvL, 123, 141101
Fattoyev, F., Piekarewicz, J., & Horowitz, C. 2018, PhRvL, 120, 172702
Ferreira, M., & Providência, C. 2019, arXiv:1910.05554
Fonseca, E., Pennucci, T. T., Ellis, J. A., et al. 2016, ApJ, 832, 167
Foreman-Mackey, D. 2016, JOSS, 1, 24
Foreman-Mackey, D., Hogg, D. W., Lang, D., & Goodman, J. 2013, PASP, 125, 306
Fortin, M., Zdunik, J. L., Haensel, P., & Bejger, M. 2015, A&A, 576, A68
Fujimoto, Y., Fukushima, K., & Murase, K. 2018, PhRvD, 98, 023019
Fujimoto, Y., Fukushima, K., & Murase, K. 2020, PhRvD, 101, 054016
Glendenning, N. K. 1997, Compact Stars: Nuclear Physics, Particle Physics, and General Relativity (New York: Springer)
Glendenning, N. K., & Moszkowski, S. A. 1991, PhRvL, 67, 2414
Guillot, S., Servillat, M., Webb, N. A., & Rutledge, R. E. 2013, ApJ, 772, 7
Güven, H., Bozkurt, K., Khan, E., & Margueron, J. 2020, arXiv:2001.10259
Hornick, N., Tolos, L., Zacchi, A., Jan-Erik, C., & Schaffner-Bielich, J. 2018, PhRvC, 98, 065804
Jiang, J.-L., Tang, S.-P., Wang, Y.-Z., Fan, Y.-Z., & Wei, D.-M. 2020, ApJ, 892, 55
Kurkela, A., Fraga, E. S., Schaffner-Bielich, J., & Vuorinen, A. 2014, ApJ, 789, 127
Lattimer, J. M., & Lim, Y. 2013, ApJ, 771, 51
Lattimer, J. M., & Prakash, M. 2007, PhR, 442, 109
Lattimer, J. M., & Swesty, F. D. 1991, NuPhA, 535, 331
Li, J. J., Sedrakian, A., & Weber, F. 2018, PhLB, 783, 234
Lindblom, L. 2010, PhRvD, 82, 103011
Logoteta, D., Vidana, I., & Bombaci, I. 2019, EPJA, 55, 207
Lonardoni, D., Lovato, A., Gandolfi, S., & Pederiva, F. 2015, PhRvL, 114, 092301
Lourenço, O., Dutra, M., Lenzi, C. H., Flores, C. V., & Menezes, D. P. 2019, PhRvC, 99, 045202
Malik, T., Alam, N., Fortin, M., et al. 2018, PhRvC, 98, 035804
Margueron, J., Hoffmann Casali, R., & Gulminelli, F. 2018a, PhRvC, 97, 025805
Margueron, J., Hoffmann Casali, R., & Gulminelli, F. 2018b, PhRvC, 97, 025806
Maslov, K. A., Kolomeitsev, E. E., & Voskresensky, D. N. 2015, PhLB, 748, 369
Miller, M. C., Lamb, F. K., Dittmann, A. J., et al. 2019, ApJL, 887, L24
Most, E. R., Weih, L. R., Rezzolla, L., & Schaffner-Bielich, J. 2018, PhRvL, 120, 261103
Nandi, R., & Char, P. 2018, ApJ, 857, 12
Nandi, R., Char, P., & Pal, S. 2019, PhRvC, 99, 052802
Nättilä, J., Miller, M. C., Steiner, A. W., et al. 2017, A&A, 608, A31
Negreiros, R., Tolos, L., Centelles, M., Ramos, A., & Dexheimer, V. 2018, ApJ, 863, 104
Oertel, M., Hempel, M., Klähn, T., & Typel, S. 2017, RvMP, 89, 015007
Özel, F., & Freire, P. 2016, ARA&A, 54, 401
Özel, F., Psaltis, D., Guver, T., et al. 2016, ApJ, 820, 28
Raithel, C. A., & Özel, F. 2019, ApJ, 885, 121
Raithel, C. A., Özel, F., & Psaltis, D. 2017, ApJ, 844, 156
Read, J. S., Lackey, B. D., Owen, B. J., & Friedman, J. L. 2009, PhRvD, 79, 124032
Riley, T. E., Watts, A. L., Bogdanov, S., et al. 2019a, ApJL, 887, L21
Riley, T. E., Watts, A. L., Bogdanov, S., et al. 2019b, A NICER View of PSR J0030+0451: Nested Samples for Millisecond Pulsar Parameter Estimation, v1.1.0, Zenodo, doi:10.5281/zenodo.3386449
Sagert, I., Tolos, L., Chatterjee, D., Schaffner-Bielich, J., & Sturm, C. 2012, PhRvC, 86, 045802
Sarin, N., Lasky, P. D., & Ashton, G. 2020, PhRvD, 101, 063021
Shen, H., Toki, H., Oyamatsu, K., & Sumiyoshi, K. 1998, NucPh, A637, 435
Steiner, A. W., Heinke, C. O., Bogdanov, S., et al. 2018, MNRAS, 476, 421
Steiner, A. W., Hempel, M., & Fischer, T. 2013, ApJ, 774, 17
Steiner, A. W., Lattimer, J. M., & Brown, E. F. 2010, ApJ, 722, 33
Steiner, A. W., Lattimer, J. M., & Brown, E. F. 2016, EPJA, 52, 18
Typel, S., & Wolter, H. H. 1999, NucPh, A656, 331
Watts, A. L., Yu, W., Poutanen, J., et al. 2019, SCPMA, 62, 29503
Weissenborn, S., Chatterjee, D., & Schaffner-Bielich, J. 2012a, PhRvC, 85, 065802
Weissenborn, S., Chatterjee, D., & Schaffner-Bielich, J. 2012b, NucPh, A881, 62
Weissenborn, S., Sagert, I., Pagliara, G., Hempel, M., & Schaffner-Bielich, J. 2011, ApJL, 740, L14
Xie, W.-J., & Li, B.-A. 2019, ApJ, 883, 174
Zhang, N.-B., & Li, B.-A. 2019, JPhG, 46, 014002